Astronomy & Astrophysics manuscript no. main
October 1, 2025

The SRG/eROSITA All-Sky Survey.

Detection of shock-heated gas beyond the halo boundary into the accretion region

X. Zhang[1], E. Bulbul[1], B. Diemer[2], Y. E. Bahar[1], J. Comparat[1], V. Ghirardini[3], A. Liu[4, 1], N. Malavasi[1], T. Mistele[1], M. Ramos-Ceja[1], J. S. Sanders[1], Y. Zhang[1], E. Artis[1], Z. Ding[1], L. Fiorino[1], M. Kluge[1], A. Merloni[1], K. Nandra[1], and S. Zelmer[1]

[1] Max Planck Institute for Extraterrestrial Physics, Giessenbachstrasse 1, 85748 Garching, Germany
e-mail: xzhang@mpe.mpg.de
[2] Department of Astronomy, University of Maryland, College Park, MD 20742, USA
[3] INAF, Osservatorio di Astrofisica e Scienza dello Spazio, via Piero Gobetti 93/3, I-40129 Bologna, Italy
[4] Institute for Frontiers in Astronomy and Astrophysics, Beijing Normal University, Beijing 102206, China

Received —; accepted —

ABSTRACT

The hot gas in the outskirts of galaxy cluster-sized halos, extending around and beyond the virial radius into nearby accretion regions, remains among one of the least explored baryon components of large-scale cosmic structure. We present a stacking analysis of 680 galaxy clusters located in the western Galactic hemisphere, using data from the first two years of the *Spectrum-Roentgen-Gamma*/eROSITA All-Sky Survey. The stacked X-ray surface brightness profile reveals a statistically significant signal extending out to $2r_{200m}$ ($\sim$ 4.5 Mpc). The best-fit surface brightness profile is well described by a combination of terms describing orbiting and infalling gas, with a transition occurring around r_{200m}. At this radius, the best-fit gas number density is 2.5×10^{-5} cm^{-3}, corresponding to a baryon overdensity of 30. By integrating the gas density profile out to r_{200m}, we infer a gas fraction of 90% of the universal baryon fraction with the assumption of a typical halo concentration, indicating the completeness of the baryon budget within large radii. Additionally, we examine the hot gas distribution in massive clusters in the IllustrisTNG simulations from the halo center to the accretion region. This analysis reveals differences in radial gas profiles depending on whether the direction probes voids or nearby cosmic filaments. Beyond r_{200m}, the density profile along the filament direction exceeds that along the void direction. This pattern aligns with the observed transition radius between the one-halo and two-halo terms, suggesting that r_{200m} is the approximate radius marking the location at which cosmic filaments connect to galaxy clusters. Meanwhile, the comparisons of the gas density profile and gas fraction profile between the observation and the IllustrisTNG simulation suggest that the feedback processes in the stacking sample are more efficient than the IllustrisTNG model in distributing gas to large radii.

Key words. Galaxies: clusters: general – Galaxies: clusters: intracluster medium – X-rays: galaxies: clusters – Large-scale structure of Universe

. Introduction

alaxy clusters, the most massive collapsed dark matter halos n the Universe, are positioned at the nodes of the cosmic web. alaxy clusters comprise $T > 10^7$ K hot baryonic gas as one ixth of their total mass and the remaining dark matter. While the ravitational potential is governed by the dark matter, baryonic hysics determines the hot gas properties. The cluster outskirts, here defined as the regions beyond r_{500c}[1], are of particular interest as they hold critical information about both the distribution of dark matter and the thermodynamic state of the gas.

The radial density profile in the outskirts is characterized by halo mass accretion, for which the behaviors of dark matter and baryons are different due to their collisional/collisionless nature (Bertschinger 1985). In the case of collisionless dark matter, the infalling matter accumulates near the first apocenter of its orbit (e.g., Fillmore & Goldreich 1984; Bertschinger 1985; Adhikari et al. 2014). This leads to a phenomenon known as splashback, where the accreted matter causes a sharp decline in the outer density profile at radii around or beyond r_{200m}. The exact location of this splashback radius is closely linked to the matter accretion rate (e.g., Diemer & Kravtsov 2014; Diemer et al. 2017a). On the other hand, infalling collisional gas forms accretion shocks[2] (e.g., Bertschinger 1985; Ostriker & McKee 1988; Shi 2016), heating the cool intergalactic medium (IGM) to $T \gtrsim 10^6$ K and creating a turbulent atmosphere outside the splashback radius (Aung et al. 2021). In reality, the distribution and thermodynamic properties of shock-heated gas[3] are more complex than

[1] Throughout this paper, we use spherical overdensity to define the mass and radius of a halo. For example, r_{500c} is the radius where the enclosed density is 500 times of critical density ρ_c; M_{200m} is the total mass enclosed by r_{200m}, where the enclosed density is 200 times of the mean matter density ρ_m.

[2] We follow the convention and use the term "accretion shock" to refer to the "external shock" in Ryu et al. (2003). In fact, the accretion shock is around all overdense environments, including cosmic filaments and sheets. In this work, we focus on the accretion shock around galaxy clusters.

[3] The terms of the intracluster medium (ICM) and warm-hot intergalactic medium (WHIM) are usually used for the hot gas in galaxy

suggested by the self-similar spherical collapse scenario, for example, because they are subject to nonthermal pressure support, infalling gas from cosmic filaments, merging, and kinetic feedback from the halo center. Fig. 1 demonstrates the X-ray emission from the hot shock-heated gas in and around a massive halo from a numerical simulation. It shows that the shock-heated gas fills the vast space in the outskirts and beyond. At radii beyond r_{200m}, the hot gas distribution is complicated by the presence of small halos falling onto the central halo. At even larger radii, the accretion shock confines the hot gas, and cosmic filaments connect the halo to the large-scale structure.

X-rays and the Sunyaev-Zeldovich effect (SZ) are the two key observational techniques to explore the hot gas properties in the outskirts (see Reiprich et al. 2013; Walker et al. 2019, for reviews). Due to the rapidly declining X-ray surface brightness and SZ Compton-y signal at large radii, most outskirt hot gas studies are limited to radii within r_{200c} (e.g., Simionescu et al. 2011; Walker et al. 2013; Eckert et al. 2013; Planck Collaboration et al. 2013; Bulbul et al. 2016; Ghirardini et al. 2019; Mirakhor & Walker 2020; McCall et al. 2024). Beyond that radius, the gas clumping (Nagai & Lau 2011; Zhuravleva et al. 2013; Eckert et al. 2015; Angelinelli et al. 2021; Zhu et al. 2023), the connection between clusters and cosmic filaments (Rost et al. 2021; Gouin et al. 2022; Malavasi et al. 2020, 2023), and the location of the accretion shock (Lau et al. 2015; Baxter et al. 2021) are poorly constrained by individual pointing observations.

Recently, several stacking analyses of X-ray and SZ survey data demonstrate high S/N in the stacked profiles beyond r_{200c}. In particular, Anbajagane et al. (2022, 2024) stacked Atacama Cosmology Telescope and South Pole Telescope SZ survey data and discovered a 6σ pressure deficit with respect to the best-fit model at $\sim r_{200m}$. Lyskova et al. (2023, hereafter L23) stacked 38 *Planck* SZ selected clusters (Planck Collaboration et al. 2016a; CHEX-MATE Collaboration et al. 2021) using the eastern Galactic hemisphere eROSITA All Sky Survey (eRASS) X-ray data, and obtained a gas density profile out to $3 \times r_{500c}$.

In this work, we stacking the western Galactic hemisphere eRASS data for more than 500 low-redshift clusters from a well-defined X-ray selected cluster catalog detected in the first All-Sky Survey (Bulbul et al. 2024; Kluge et al. 2024). The larger sample allows us to investigate the circumcluster hot gas properties out to a larger radius. This article is organized as follows: in Sect. 2 we present the sample and the stacking analysis; we model the stacked profile in Sect. 3 ; in Sect. 4 we use the numerical simulations to validate the stacking and modeling results; discussion and conclusion are presented in Sects. 5 and 6, respectively. We adopt a flat Lambda-Cold-Dark-Matter cosmology with parameters $H_0 = 70$ km s^{-1} Mpc^{-1}, $\Omega_m = 0.3$, and $\Omega_\Lambda = 0.7$. The cosmic baryon fraction is adopted from Planck Collaboration et al. (2020), where $\Omega_b/\Omega_m = 0.158$.

2. Observation sample and data reduction

2.1. Sample selection

We select our analysis sample from the first half-year survey of eRASS (hereafter eRASS1) primary galaxy clusters and groups catalog (Bulbul et al. 2024), which is based on extended sources

clusters and cosmic filaments, respectively. Both gases are heated by cosmic accretion shocks when accreted onto the cosmic web. At the radii where halos are connected with cosmic filaments, there is no clear boundary to distinguish the ICM and WHIM. Therefore, in this work, we use the term "shock-heated gas" to refer to the hot gas in both halos and cosmic filaments.

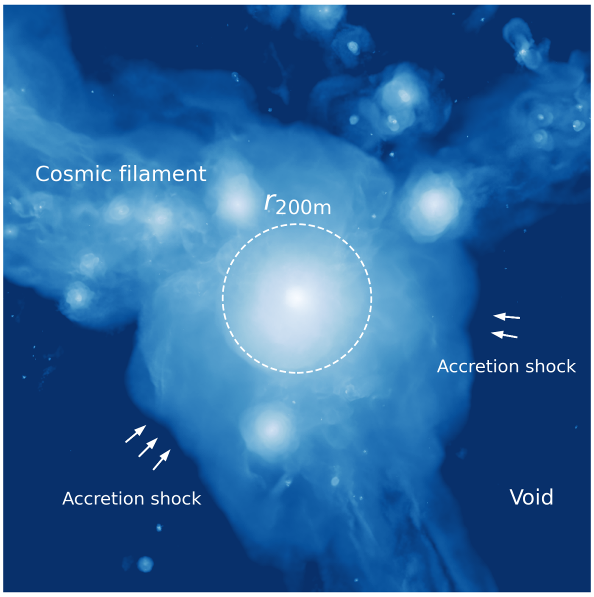

Fig. 1. Spatial distribution of the X-ray emission from the hot gas around a massive dark matter halo. The dashed circle indicates the size of r_{200m}. At large radii, the halo is connected to and accreting smaller nearby halos from cosmic filaments. This map is produced using gas particles from a $20 \times 20 \times 20$ Mpc^3 box around the `id=32` halo in the $z = 0$ snapshot of the TNG300-1 simulation (see Sect. 4 for the details of map creation). The central halo is in a mass $M_{500c} = 2.8 \times 10^{14} M_\odot$ and an r_{200m} of 2.5 Mpc. Short arrows mark the accretion shock, i.e., the boundary between shock-heated gas and the cool intergalactic medium.

in the eRASS1 primary catalog (Merloni et al. 2024) with further optical confirmation (Kluge et al. 2024). The overdensity masses M_{500c} of the clusters were estimated using the 0.2–2.3 keV count rate to the weak lensing calibrated mass scaling relation from the eRASS1 cluster abundance cosmology analysis (Ghirardini et al. 2024; Grandis et al. 2024; Kleinebreil et al. 2025; Okabe et al. 2025). We selected a luminosity-limited sample in the low redshift Universe based on the following criteria:

1. Luminosity $L_{0.5-2\mathrm{keV}} > 2 \times 10^{43}$ erg s^{-1}, which corresponds to a mass threshold of $M_{500c} \approx 2 \times 10^{14} M_\odot$ based on the scaling relations from the eRASS1 cosmology;
2. Redshift $0.03 < z < 0.2$;
3. Optical richness $\lambda > 20$ to eliminate left over contamination in the sample;
4. Galactic latitude $|b| > 20°$ to avoid high galactic absorption;
5. The median value of the 0.6–1 keV band count rate (Zheng et al. 2024) in a 0.5°–3° annulus < 6 cts s^{-1} deg^{-2} to avoid high Galactic foreground emission;
6. At least a 3.5° angular distance to the eROSITA-DE footprint boundary for proper stray light estimation (see Sect. 2.2.2).

With the criteria above, we selected 694 clusters of galaxies. We visually checked their locations on the sky map. Two objects are affected by the Virgo Cluster emission and are therefore removed. Twelve objects were removed because they are the less massive clusters in cluster pairs. After this process, a sample of 680 clusters remains in a redshift range of 0.034 to 0.2 and a M_{500c} range of $1.3 - 11.6 \times 10^{14} M_\odot$. The median values of the sample redshift and M_{500c} are 0.15 and $2.6 \times 10^{14} M_\odot$, respectively. The mass-redshift distribution, as well as the sky position distribution of the sample are plotted in Fig. 2. It shows that the 0.6–1 keV count rate threshold we applied successfully selects objects in low foreground emission regions.

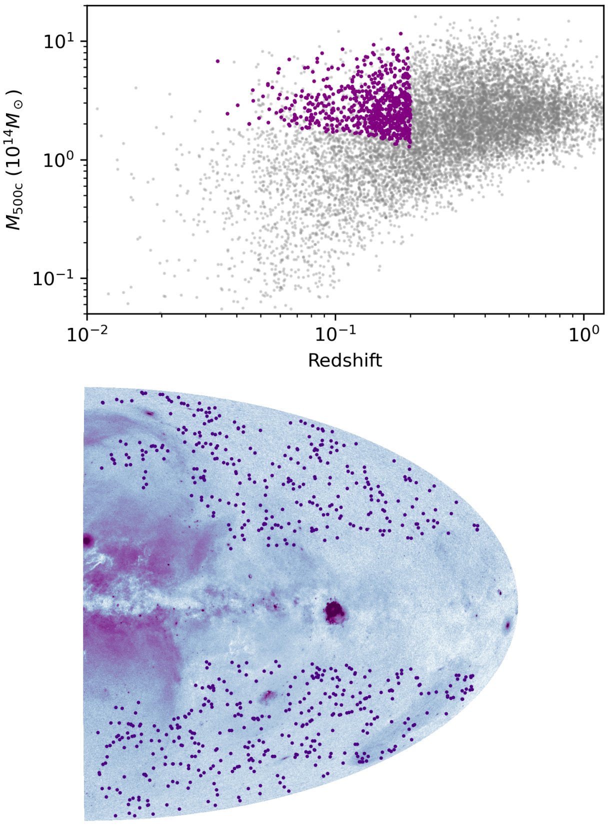

Fig. 2. *Top*: Mass-redshift distribution of the full eRASS1 galaxy cluster and group sample (gray) from (Bulbul et al. 2024) and the clusters used in this work (purple). *Bottom*: Locations of the selected sample on the west Galactic hemisphere eRASS1 X-ray sky.

2.2. Data reduction and surface brightness profile stacking

We analyze the first four scans of eROSITA All-Sky Survey (hereafter eRASS:4) data, which were collected from 12th December 2019 to 19th December 2021. The data were processed with the eSASS (Brunner et al. 2022) pipeline version 020, which is similar to the version 010 used for eRASS1 data release with improvements on boresight correction, detector noise suppression, and subpixel position computation (see Merloni et al. 2024, for the details). We only select the events from telescope modules (TMs) 1,2,3,4,6 (hereafter TM8) to avoid the systematic uncertainties caused by the optical light leak in TMs 5 and 7 (Predehl et al. 2021). We used the tools in the software package eSASS version `eSASSusers_211214_0_4` to generate eRASS data products.

For each cluster, we extracted the 0.2–2.3 keV TM8 count image using `evtool` and generated the corresponding vignetting corrected exposure map using `expmap`. The count map and exposure map are centered at the cluster X-ray centroid and are extended to an angular distance of $10 \times r_{500c} + 3.5°$, where the $10 \times r_{500c}$ aperture is used for analysis and the additional 3.5° annulus is for calculating the stray light from the sources outside the analysis region.

2.2.1. Source masks

We masked out different types of sources for each cluster field. These sources include

1. X-ray point sources in eRASS:4 catalog, where the source detection method and analysis are described in Merloni et al. (2024). We note that in a cluster field, especially in the central bright region, the source detection configuration used for the master catalog returns spurious point source entries (Merloni et al. 2024). We cleaned these spurious sources by running an additional wavelet detection process in the $r < r_{500}$ region. We first ran the software WVDECOMP[4] with both detection and filtering thresholds $(3, 3, 3, 4, 4)$ at scales $(8, 16, 32, 64, 128)''$. Then we ran the software SEXTRACTOR on the wavelet-filtered image to identify sources, where we adopted a detection threshold of 10. We cross-matched the wavelet-detected sources with those in the eRASS:4 master catalog. In the $r < 0.8 \times r_{500c}$ region, we only masked out sources identified by both methods.
2. Galaxy clusters and groups. We followed Zhang et al. (2024) to mask out 1) X-ray selected galaxy clusters and groups in the eRASS1 cluster catalog (Bulbul et al. 2024) with masking radii $1.5 r_{500c}$; and 2) optically selected richness $\lambda > 20$ clusters[5] with masking radii $1.5 r_\lambda$ (see eq. 4 in Rykoff et al. 2014 for definition).

2.2.2. Stray light

The cluster emission in the regions we are interested in is below the sky background. Therefore, the stray light of eROSITA, which is the 3.5° radius halo around any source produced by single reflected photons, could have an impact on the stacked profile and needs to be removed. We follow the recipe described in appendix A of Churazov et al. (2023) to correct for the stray light contamination. In short, for each object, we first estimate the sky background level by taking the average count rate of the source-free region. Then we convolve the sky background-subtracted and vignetting-corrected count rate image with a kernel of the stray light profile (eq. A.2 in Churazov et al. 2023) to obtain a first-order approximation of the stray light count rate. The normalization of the stray light kernel is computed as the fraction of the 2D stray light profile volume with respect to the 2D volume of the total point spread function (PSF) (eq. A.1 + eq. A.2 in Churazov et al. 2023).

2.2.3. Profile stacking

The image products we created have pixel widths of 8″, resulting in a total number of 6.5×10^8 pixels for stacking. Meanwhile, this pixel size is smaller than the 30″ PSF half-energy width of the eRASS. To boost the calculation speed and save the memory space, we binned the original pixels to a $N_{\rm side} = 4096$ hierarchical equal area isolatitude pixelisation (HEALPix) scheme following the method described in Zhang et al. (2024).

For each object, we extracted a count number profile and an exposure profile from the count map and exposure map, respectively. The radii of the profiles are scaled to r_{200m} of the object, which was converted from r_{500c} by assuming an Navarro-Frenk-White (NFW) profile with the halo concentration parameter $c_{200c} = 4$. This value approximately represents the concentration of halos in the cluster mass range of the sample (e.g. Child et al. 2018; Diemer & Joyce 2019; Ishiyama et al. 2021; Okabe et al. 2025). The conversion factor has a redshift dependence,

[4] https://github.com/avikhlinin/wvdecomp
[5] It is a proprietary catalog of redMaPPer (Rykoff et al. 2014) run on the DESI Legacy Imaging Surveys (Dey et al. 2019) DR10 data. See Kluge et al. (2024) for the description.

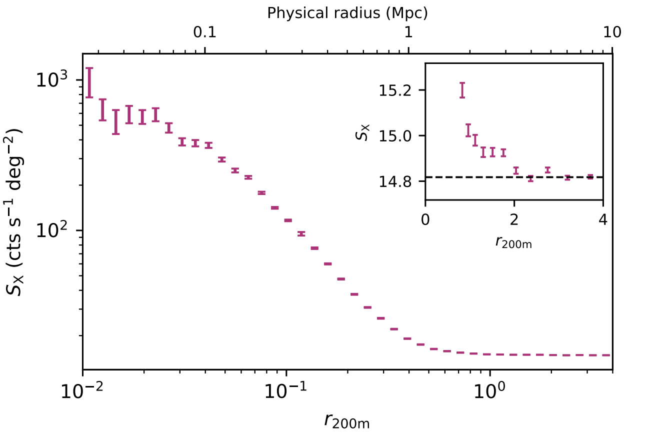

Fig. 3. The stacked eROSITA surface brightness profile in the 0.2–2.3 keV band after the stray light component has been removed. The radial distance to the cluster center is scaled to the overdensity radius r_{200m}. The corresponding physical radius given the sample median mass and redshift is labeled at the top of the figure. The top-right inset provides a zoomed-in view of the profile within a zoomed surface brightness range around the background level, with the dashed horizontal line indicating the average surface brightness between 3 and 4 r_{200m}. The profile shows significant X-ray emission extended to approximately $2 \times r_{200m}$.

ranging from 2.48 at $z = 0.034$ to 2.24 at $z = 0.2$ within our sample.

We stacked the surface brightness profiles using a projected sky solid angle weighted method. The weight of each object $w = D_A^2 r_{500c}^{-2}$ corrects for the potential bias from nearby objects and massive objects that are of a large angular size, where D_A is the angular diameter distance as a function of redshift. The stacked surface brightness profile is

$$S_X(r) = \frac{\sum_i w_i N_i(r)}{\sum_i w_i t_i(r) \Omega_i(r)}, \tag{1}$$

where $N_i(r)$ the ith count profile, $t_i(r)\Omega_i(r)$ the ith exposure profile in unit of s^{-1} deg^{-2}. We used the HEALPix oriented bootstrap resampling method described in Zhang et al. (2024) to estimate the uncertainty of the stacked profile. We created 500 bootstrapping samples of the HEALPix pixels from the full pixel list, and for each bootstrapping sample, we calculated a stacked profile using Eq. 1. Throughout this paper, we use the mean and covariance matrix of the 500 bootstrapping sample profiles to represent the stacked profile and its uncertainty.

3. Stacked eROSITA surface brightness profile and modeling

The stacked profile of the 680 galaxy clusters from 0.01 to 4 r_{200m} is shown in Fig. 3. As expected, the background level is consistent with the values in the 0.2-2.3 keV reported by Zheng et al. (2024), which is $\sim$ 15 cts s^{-1} deg^{-2} in the Galactic anticenter region with the instrumental background included. The high S/N of the stacked profile allows us to probe the extremely weak signal at the background-dominant radii. The inset in Fig. 3 shows that there is still a significant positive signal above the local background level at $r > r_{200m}$. Based on bootstrap sampling, the averaged surface brightness in the 1-2 r_{200m} range is higher than in the 2-4 r_{200m} range with a significance of 12σ. We conclude that this constitutes a significant detection of the signal up to $2 \times r_{200m}$, which is approximately 4.5 Mpc given the median mass and redshift ranges of our sample. At $\sim 2 \times r_{200m}$, there is a plausible bump. We investigate it by separating each cluster into four 90° sectors and stacking each of the sectors (see Appendix A). We found that this feature is contributed by the fluctuation in the first sector and is not universal in all sectors. Meanwhile, in Appendix B, we perform a test of stacking signals with cluster positions randomly distributed on the sky. This experiment shows that the uncertainty from uncorrelated components is less than 0.3% of the background level. The test indicates that the detected signal does not arise from a background fluctuation in this background-dominated regime, but instead originates from X-ray emission in the circumcluster accretion region. In the following subsections, we model the stacked surface brightness profile in the full radial range out to $4 r_{200m}$.

3.1. Model formalism

Numerical simulations suggest that both the dark matter and gas density profiles from halo center to a few r_{200m} can be separated as inner and outer parts (e.g., Diemand & Kuhlen 2008; O'Neil et al. 2021; Diemer 2022; García et al. 2023). The inner profile is contributed by the matter orbiting within the halo, and the outer profile is contributed by infalling matter in the ambient accretion region, e.g., nearby cosmic filaments and halos therein. The transition between the two regions is characterized by a sharp change in slope. This feature has been observed in SZ stacking (e.g. Anbajagane et al. 2022, 2024) and weak lensing shear stacking (e.g. Chang et al. 2018).

Numerous models for the inner and outer profiles have been proposed, some of which we later test in Section 4.1. For the purpose of fitting our observed data, we adopt a relatively simple prescription based on the halo model that is commonly used to describe large-scale clustering (see Cooray & Sheth 2002, for a review). Specifically, for the one-halo term, we adopt a generalized NFW (gNFW) profile,

$$n_H^{\rm gNFW}(r) = n_{H,0} \times \frac{1}{(r/r_s)^\gamma \left[1 + (r/r_s)^\alpha\right]^{(\beta-\gamma)/\alpha}}, \tag{2}$$

where α, β, γ, and r_s are the four shape parameters. The gNFW model has been widely used for describing the pressure profile of cluster gas (e.g. Nagai et al. 2007; Arnaud et al. 2010; Bulbul et al. 2010). Because the X-ray emitting gas in the off-filament directions terminates at the accretion shock, we additionally add this feature to the model. We assume that the hot gas density in the downstream region after shock compression is the mean baryon density $\langle \rho_b \rangle$. The modified hydrogen density profile is then

$$n_H(r) = \begin{cases} n_H^{\rm gNFW}(r) & n_H(r) \geq \langle n_H \rangle \\ 0 & \text{elsewhere,} \end{cases} \tag{3}$$

where $\langle n_H \rangle$ is the mean hydrogen number density converted from $\langle \rho_b \rangle$. For our observed sample, $\langle n_H \rangle = 3 \times 10^{-7}$ cm^{-3} at the sample's median redshift of 0.15. The gas density can be converted to an X-ray emission

$$\epsilon_{1h}(r) = n_e n_H \Lambda_{cf}(T, Z), \tag{4}$$

where we adopt $n_e = 1.2 n_H$ for the hot gas and $\Lambda_{cf}(T, Z)$ is the temperature and metalicity-dependent cooling function. We projected the 3D emission onto a 2D plane. The projected surface X-ray photon rate is

$$\Sigma_X(r) = 2 \times \int_0^{l_{max}} \epsilon_X \left(\sqrt{l^2 + r^2} \right) dl, \tag{5}$$

where l is the projection line of sight (LOS), $l_{\rm max}$ is the one side projection depth. With a flat sky approximation, the observed surface brightness

$$S_{\rm X}\left[{\rm cts\ s^{-1}\ deg^{-2}}\right] = \Sigma_{\rm X}\left[{\rm cts\ s^{-1}\ kpc^{-2}}\right] \times A_{\rm eff}\left[{\rm cm^2}\right] \times \frac{2.55\times10^{-48}}{(1+z)^3}, \quad (6)$$

where $A_{\rm eff}$ is the averaged effective area of the observation band. We calculated $\Lambda_{\rm cf}A_{\rm eff}$ in the 0.2–2.3 keV band 1) using the APEC model with ATOMDB v3.09 (Smith et al. 2001; Foster & Heuer 2020), 2) with an assumption of $Z = 0.3Z_\odot$ and Lodders et al. (2009) abundance table, 3) using the effective area curve of the five used eROSITA telescope modules, 4) applying a K-correction at $z = 0.15$, and 5) taking an averaged foreground the average HI column density of 3×10^{20} cm^2 of the sample into account. The value of $\Lambda_{\rm cf}A_{\rm eff}$ varies between 3 and 6 ph s^{-1} cm^5 in the temperature range $T > 3\times10^6$ K. In this work, we adopted $\Lambda_{\rm cf}A_{\rm eff} = 4.9\times10^{-12}$ ph s^{-1} cm^5, which is the averaged value in the $3\times10^6 - 5\times10^7$ K temperature range. If a $Z = 0.2Z_\odot$ assumption is applied, the averaged value will be slightly decreased by 20%, which is mainly due to the less contribution of line emission in $T \lesssim 1.5\times10^7$ K.

For the two-halo term, we started with theoretical calculations of the X-ray emission from nearby halos that are spatially correlated with the central halo. The distribution of neighbor halos around a halo can be described

$$\frac{{\rm d}n}{{\rm d}V}(r, M_{\rm c}) = \xi^{\rm lin}_{\rm mm}(r)b(M_{\rm c})\int\frac{{\rm d}n}{{\rm d}M{\rm d}V}b(M){\rm d}M, \quad (7)$$

where $M_{\rm c}$ is the mass of the central halo, $\xi^{\rm lin}_{\rm mm}$ is the matter-matter correlation function in the linear regime, ${\rm d}n/{\rm d}M{\rm d}V$ is the halo mass function (HMF), b is the mass dependent halo bias parameter, which quantifies the excess clustering of halos over the clustering of dark matter. We adopted HMF from Tinker et al. (2008) and halo bias from Tinker et al. (2010). The profile of $\xi^{\rm lin}_{\rm mm}$ and the models of halo bias and HMF are numerically implemented in the package colossus[6] (Diemer 2018). With a halo luminosity-mass scaling relation, we converted the halo distribution to the emission distribution,

$$\epsilon_{\rm 2h}(r, M_{\rm c}) = \xi^{\rm lin}_{\rm mm}(r)b(M_{\rm c})\int_{M_{\rm min}}^{M_{\rm max}}\frac{{\rm d}n}{{\rm d}M{\rm d}V}b(M)L_{\rm X}(M){\rm d}M, \quad (8)$$

where $\epsilon_{\rm 2h} \equiv {\rm d}L_{\rm X,2h}/{\rm d}V$, $L_{\rm X}(M)$ is the luminosity-mass scaling relation, $M_{\rm min}$ and $M_{\rm max}$ are the integration limits. We used a survey selection function to describe the halo masking. Therefore, we rewrote Eq. 8 to

$$\epsilon_{\rm 2h}(r, M_{\rm c}, z) = \xi^{\rm lin}_{\rm mm}(r,z)b(M_{\rm c},z) \times\int_0^{M_{\rm max}}\frac{{\rm d}n(M,z)}{{\rm d}M{\rm d}V}b(M,z)\left[1-\mathcal{D}(M,z)\right]L_{\rm X}(M,z){\rm d}M, \quad (9)$$

where $\mathcal{D}(M,z)$ is the eRASS1 X-ray selection function (Clerc et al. 2024), $M_{\rm max}$ is the mass threshold of masking objects in observations, which is approximately $10^{14.3}M_\odot$ given our $\lambda = 20$ richness threshold for source masking and the richness-mass scaling relation from Ghirardini et al. (2024). For the $L_{\rm X} - M$ scaling relation, we adopted the one from Bulbul et al. (2019) and applied a factor of 1.4 to convert 0.5–2 keV luminosity to 0.2–2.3 keV luminosity. Similar to the one-halo component, we applied Eqs. 5 and 6 to $\epsilon_{\rm 2h}$ to obtain the projected two-halo term model surface brightness, where we used an integration limit $l_{\rm max}$ = 100 Mpc. We created the individual object two-halo model, and then stacked them using Eq. 1 to obtain a synthesis model $S^{\rm 2h}_{\rm X,halo}(r)$ for fitting. To account for the emission from unvirialized filament gas, an additional free normalization parameter $A_{\rm 2h}$ is also included in the fitting. The final projected two-halo model can be expressed as

[6] https://bdiemer.bitbucket.io/colossus

Table 1. Best-fit parameters of the gNFW gas density profile and the two-halo term normalization.

Parameter	Unit	Value
$\log n_{\rm H,0}$	cm^{-3}	-2.9 ± 0.2
$r_{\rm s}$	$r_{\rm 200m}$	1.2 ± 0.3
α	-	0.74 ± 0.05
β	-	5.7 ± 0.6
γ	-	0.39 ± 0.09
$S^{\rm 2h}_{\rm X}(r_{\rm 200m})$	cts s^{-1} deg^{-2}	0.22 ± 0.03

$$S^{\rm 2h}_{\rm X}(r) = A_{\rm 2h}S^{\rm 2h}_{\rm X,halo}(r). \quad (10)$$

We used a constant profile to account for the background components that are not associated with our stacking objects. The uncorrelated components include the instrumental background, Galactic foreground, and the cosmic X-ray background.

3.2. Surface brightness profile fitting

We modeled the stacked eRASS:4 profiles using the Bayesian inference package pocoMC (Karamanis et al. 2022a,b). The likelihood is defined as $\mathcal{L} = -\chi^2/2$, where $\chi^2 = (S^{\rm data}_{\rm x} - S^{\rm model}_{\rm x})^{\rm T}C^{-1}(S^{\rm data}_{\rm x} - S^{\rm model}_{\rm x})$ is a generalized form that takes the profile covariance into account. We applied flat priors for all parameters. We adopted the median and the 16th to 84th percentiles of the posterior as the best-fit parameter and the uncertainty range.

We fitted the model combination of the gNFW, two-halo, and a constant to the 0.2–2.3 keV stacked profile. The best-fit parameters are listed in Table 1. In Fig. 4, we plot each best-fit component of the stacked profile as well as the fit residual. The fitting illustrates that the $r_{\rm 200m}$ is approximately the boundary between the one-halo dominant and two-halo dominant regions. To check the necessity of including the two-halo term in the fitting, we also fitted the profile using `gNFW + constant` model combination. The best-fit components are plotted in Fig. C.1. Without the two-halo term, there are more residuals in the range of $1-2\times r_{\rm 200m}$. Based on the Bayesian model comparison framework, we calculated the Bayes factor of the two fits, which is exp(11.5). It suggests that the fitting by including the two-halo term is decisively favored according to the Jeffreys' scale (Jeffreys 1961) or a similar scale later suggested by Kass & Raftery (1995). The normalization of the two-halo term is 0.22 ± 0.03 cts s^{-1} deg^{-2} at $r_{\rm 200m}$, corresponding to 2×10^{35} erg s^{-1} kpc^{-2} at the sample median redshift, which is at the same order of the magnitude of that from the recent galaxy-X-ray cross-correlation study (Comparat et al. 2025).

3.3. Density profile and comparison with the literature

We present the best-fit one-halo term gas number density profile in Fig. 5. We note that the profile we show is the total gas number density $n_{\rm tot}$, where $n_{\rm tot} = 2.3\times n_{\rm H}$ for typical halo gas. We use two different ways to present the profile uncertainty: the purple band

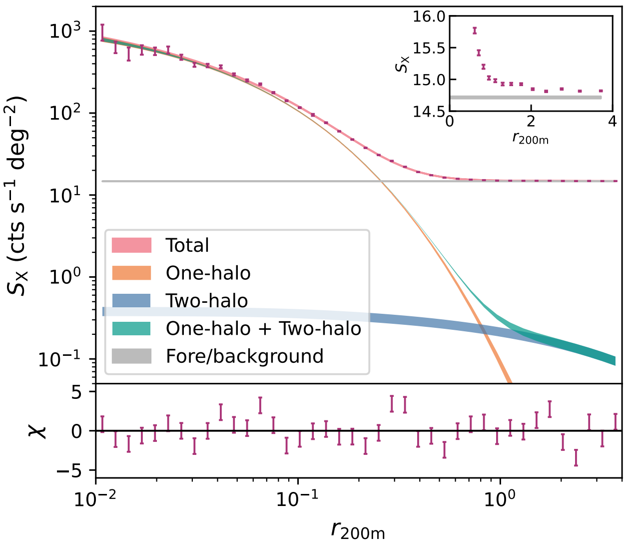

Fig. 4. Best-fit results of the stacked 0.2–2.3 keV eROSITA surface brightness profile, where we adopted the gNFW model for the one-halo component. The width of each component denotes the 1σ scatter of the posterior samples. The inset shows a zoomed-in view around the background level.

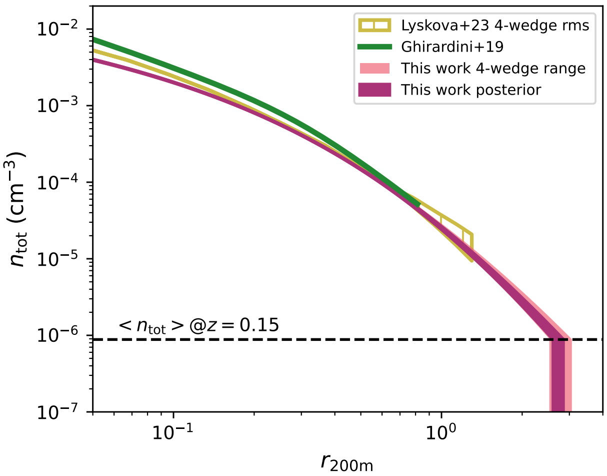

Fig. 5. Best-fit gNFW gas number density profile 1σ posterior range (purple) and the range of individual fittings of the four wedges (red) inferred by the eROSITA observations. The result from L23 (yellow) up to $3 \times r_{500c}$, and the result from Ghirardini et al. (2019) up to $2 \times r_{500c}$ (green).

is the 1σ scatter of the posterior sample from model inference; the red band is the range of the fitting results of four individual sectors. Due to the large pixel size we used for stacking, which is 0.86′, or 140 kpc physical scale at sample median redshift 0.15, we only show the density profile beyond $0.05 \times r_{200m}$. Our best-fit density profile illustrates that the gas density at a large radius of r_{200m} is still about 2.5×10^{-5} cm^{-3}, corresponding to a baryon density contrast of 30. The cutoff of the profile at the cosmic averaged baryon density is introduced by the condition we applied in Eq. 3. We discuss it later in Sect. 5.1.

Our best-fit density profile is overall consistent with the density profiles derived from the *XMM-Newton* and eROSITA observations of the *Planck*-selected samples out to two and three r_{500c}, as shown in Fig. 5 (Ghirardini et al. 2019; Lyskova et al. 2023). The normalization and slopes derived from the eROSITA observations of *Planck*-selected clusters in L23 are consistent with our fits in the radial range of $0.4 - 1 \times r_{200m}$. Nonetheless, within the central region $r < 0.4 \times r_{200m}$, we find a slightly shallower slope and lower normalization. By contrast, the density profiles from the *XMM-Newton* observations in Ghirardini et al. (2019) show the highest normalization and the steepest slope compared to both our results and those of L23. A likely explanation for the offset observed in the central regions is the different mass ranges of the utilized samples. L23 stacked eROSITA observations of the *Planck* SZ sample (Planck Collaboration et al. 2016a) with a mass threshold of $M_{500c} > 2 \times 10^{14}\ M_\odot$ and a mean mass of $4.1 \times 10^{14}\ M_\odot$, while Ghirardini et al. (2019) used the X-COP sample (Eckert et al. 2017), which consists of 12 *Planck*-selected clusters with masses significantly higher than both our sample and that of L23. Thus, both comparison samples probe higher-mass clusters than those studied in this work, which could account for the observed offset.

4. Stacked profiles in IllustrisTNG simulation

In this section, we explore the galaxy cluster halos in the IllustrisTNG simulation to 1) validate our stacking and modeling processes; 2) compare the observations to the simulations to understand underlying physical processes in this unexplored region with previous observations; 3) study the 3D structure of the shock heated gas from the galaxy cluster center to the accretion region. The IllustrisTNG is a suite of cosmological magnetohydrodynamical simulations (Naiman et al. 2018; Springel et al. 2018; Nelson et al. 2018; Marinacci et al. 2018; Pillepich et al. 2018) of galaxy formation in a fixed cosmology (Planck Collaboration et al. 2016b). Halo and galaxy catalogs are based on the friend-of-friend (FoF) algorithm and subhalo/galaxy identification with Subfind (Springel et al. 2001).

For this work, we use the $z = 0$ snapshot of the highest-resolution version on the largest box, TNG300-1, to study the X-ray properties in cluster outskirts. Specifically, we select 159 halos with $M_{500c} > 10^{14}\ M_\odot$ from the FoF catalog, whose mass range is comparable to the observation sample. We use the code HYDROTOOLS (Diemer et al. 2017b, 2018; Tacchella et al. 2019) to extract all gas cells out to 10 Mpc and calculate thermodynamic properties: (1) the total gas number density $n_{tot} = n_H + n_e + n_{He}$, the sum of hydrogen, electron, and helium number density. The n_H and n_{He} are converted from the mass density by assuming mass fractions of 0.76 and 0.24, respectively. The n_e are calculated using the electron abundance of the cell. We ignore the contribution from metal elements in the total number density. (2) the gas temperature T, which is converted from the internal energy of the gas cell. (3) the electron entropy $K_e = k_B T_e n_e^{-2/3}$, where k_B is the Boltzmann constant, $T_e = T$ by assuming the thermal equilibrium. (4) the gas pressure $P_{gas} = n_{tot} k_B T$.

In addition, we calculate the 0.2–2.3 keV X-ray emission properties by assuming a collisional ionization equilibrium condition and using the ATOMDB v3.09 APEC code (Smith et al. 2001; Foster & Heuer 2020). For each gas cell,

$$L_X = V_{cell} n_H n_e \Lambda_{Z=0}(T) + Z_{cell} V_{cell} n_H n_e \left[\Lambda_{Z=Z_\odot}(T) - \Lambda_{Z=0}(T)\right], \quad (11)$$

where V_{cell} is the cell volume, Z_{cell} is the cell metalicity in solar unit, $\Lambda_{Z=0}$ and $\Lambda_{Z=Z_\odot}$ are the cooling function with zero metalicity and solar metalicity (Lodders et al. 2009), respectively.

4.1. Projected emission profile and fitting method validation

In this subsection, we validate the profile fitting framework using the simulation data. We aim to investigate whether the fitting results from the profile modeling framework we applied in Sect. 3 could match the true 3D density profiles up to the accretion shock.

In each $20 \times 20 \times 20$ Mpc^3 boxes centered at each halo, we projected the 0.2–2.3 keV X-ray emission on the XY, YZ, and XZ planes, respectively. Then we created nearby (sub)halo masks for each object and each projection angle with M_{500c} threshold of 10^{13}, $10^{13.5}$, and 10^{14} $M_\odot$. We note that some of the bright X-ray halos in binary or multi-object systems are not identified as the main halo. We therefore excluded Subfind halos instead of FoF halos with a masking radius of $1.5r_{500c}$. Though the overdensity mass is not in the Subfind catalog, it can be converted from $M_{\rm subfind}$. For most central halos, the ratio between M_{500c} and $M_{\rm subfind}$ is about 2/3. For each projection direction and halo mask threshold, we stacked the radially averaged projected emission profile

$$\Sigma_{\rm x}(r) = \frac{\sum_i w_i \Sigma_{{\rm x},i}(r)}{\sum_i w_i}, \tag{12}$$

where r is the radius in a unit of r_{200m}, w_i is the weight, and here we adopted r_{500c}^{-2} to reduce the bias from the large physical size objects. We calculated the median profile from the three projection angles as the final stacked profile.

The stacked 0.2–2.3 keV $\Sigma_{\rm x}$ profile with the three nearby-halo masking thresholds is plotted in the left panel of Fig. 6 as shaded regions. The three stacked profiles are identical in the $r < 0.7 \times r_{200m}$ radial range and turn flat at $r \gtrsim r_{200m}$. The outer parts of the profiles are contributed by gaseous (sub)halos with masses below the masking threshold from the far outskirts to cosmic filaments, together with the unvirialized gas in filaments. Different halo masking thresholds result in different $\Sigma_{\rm x}$ normalizations of the outer profile. Meanwhile, the outer parts of the three stacked profiles show several enhancements, where the one in the $10^{14} M_\odot$ masking threshold profile is the most significant. These enhancements are from bright X-ray halos that are below the masking threshold, and as the threshold decreases, the significance of these enhancements to the overall emission becomes negligible.

We followed Sect. 3 to fit the one-halo and two-halo models to the projected 2D simulated $\Sigma_{\rm X}$ profiles. For the one-halo term, in addition to the gNFW model we used in Sect. 3, we include two more models for testing:

– The Vikhlinin et al. (2006, hereafter V06) profile, which is

$$n_{\rm H} = n_{\rm H,0} \times \frac{(r/r_{\rm c})^{-\alpha}}{[1+(r/r_{\rm c})^2]^{3\beta-\alpha/2}} \times \frac{1}{[1+(r/r_{\rm s})^\gamma]^{\epsilon/\gamma}}\,, \tag{13}$$

where $n_{\rm H,0}$ is the hydrogen number density normalization, α, β, ϵ, γ, $r_{\rm c}$, and $r_{\rm s}$ are the six parameters that control the profile shape.

– The L23 profile, which is a modification of the V06 profile with an additional slope change at the large radii,

$$n_{\rm H} = n_{\rm H,0} \times \frac{(r/r_{\rm c})^{-\alpha}}{[1+(r/r_{\rm c})^2]^{3\beta-\alpha/2}} \times \frac{1}{[1+(r/r_{\rm s})^\gamma]^{\epsilon/\gamma}} \times \frac{[1+(r/r_{\rm s2})^\gamma]^{\epsilon/\gamma}}{[1+(r/r_{\rm s2})^\xi]^{\lambda/\xi}}\,, \tag{14}$$

where λ, ξ, $r_{\rm s2}$ are three additional shape parameters.

We adopted a constant value $\Lambda_{\rm cf} = 8 \times 10^{-24}$ erg s^{-1} cm^3 by assuming a constant temperature and abundance profile for the density to emissivity conversion. This is approximately the radiative cooling in the 0.2–2.3 keV band with $T = 2 \times 10^7$ K and $Z = 0.3Z_\odot$. As discussed in Sect. 3, a choice of a lower metalicity of $0.2Z_\odot$ could result in a slightly lower $\Lambda_{\rm cf}$. For the two-halo term formalism, there are several settings different from those we used in Sect. 3.1. First, we adopt the TNG300-1 $L_{\rm X} - M$ scaling relation from Pop et al. (2022). Second, because the simulation data we extracted for each cluster are in $20\times20\times20$ Mpc^3 boxes, we used $l_{\rm max} = 10$ Mpc as the one side projection depth when calculating the model $\Sigma_{\rm X}$ using Eq. 5. Third, because we masked nearby halos in simulations only based on the mass, we did not further apply additional selection functions such as the one in Eq. 9.

We fit the three stacked profiles with the different mass exclusion thresholds, with the combined one-halo and two-halo terms. For each stacked profile, the three one-halo models are used separately for validation. We used the package IMINUIT (Dembinski et al. 2020) for minimizing the χ^2 values. The left panel of Fig. 6 shows the results of the fits with the gNFW model as the one-halo component. The middle panel of Fig. 6 presents the residuals and best-fit χ^2 values of the fits using the gNFW, V06 and L23 models on the three stacked profiles with different mass exclusion thresholds. The residuals show that all three one-halos models, together with the two-halo term, can well fit the projected emission profile from halo center to $4 \times r_{200m}$. The three one-halo profile models return similar residuals and χ^2 values. The large residual in fittings with a nearby halo masking threshold of 10^{14} $M_\odot$ is due to several unmasked bright objects that are below the threshold. The right panel of Fig. 6 shows the best-fit one-halo density profiles of the gNFW, V06, and L23 models in dashed, dashed-dotted, and dotted lines, respectively, where different colors denote the different nearby halo masking thresholds. We overplot the scatter of the 3D density profiles in the off-filament directions as the gray shaded region (see later Sect. 4.3 for details). All the best-fit 3D density profiles using the three models are close to the true profiles. Among the three models we tested, the L23 model exhibits the most scatter, due to its additional flexibility of changing the slope at the large radii. Meanwhile, the fits using the gNFW model are in good agreement with those using the V06 model, despite having two fewer shape parameters. This comparison also highlights that the gNFW model can well describe the gas density profile to a large radius. Complex models with more shape parameters do not significantly improve the fitting residual.

This analysis shows that by adding a two-halo term to account for the nearby infalling (sub)halos and circumcluster gas in the cosmic filament directions, all three one-halo density models can well recover the true density profile in the off-filament directions out to the accretion shock in numerical simulations. In other words, the two-halo term accounts for the major gas-clumping effects, i.e., the presence of nearby (sub)halos and isotropic gas distribution due to cosmic filaments at large radii. The mild offset between the best-fit profile normalization and the median of the true 3D density profile can be explained by other minor clumping effects, e.g., halo triaxiality, density fluctuations due to turbulence, and the presence of inner shock and cold fronts. Moreover, even if we assumed a constant cooling function and ignored the variation of temperature and metalicity, the fits successfully recover the true number density profile, suggesting a minor impact from the two effects. We therefore conclude that our models, validated against the IllustrisTNG simula-

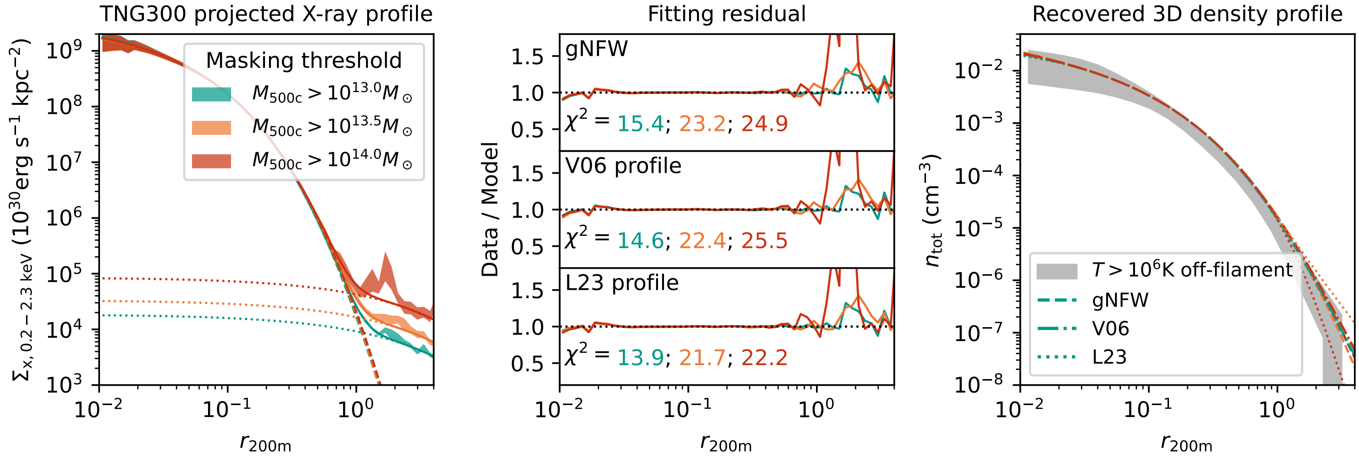

Fig. 6. *Left*: Stacked surface X-ray emission profiles of the TNG300-1 galaxy cluster halos. The teal, orange, and red colors denote the nearby-halos masking thresholds of 10^{13}, $10^{13.5}$, and $10^{14} M_\odot$, respectively. The shaded regions are the sample bootstrapping uncertainties that reflect the sample scatter. The best-fit of the gNFW profiles, the two-halo terms, and the total profiles are plotted in the dashed, dotted, and solid lines, respectively. The sharp peaks in the outer profile are contributed to by bright nearby halos that are below the masking threshold. *Middle*: The residuals of the fittings of the three different one-halo models. The χ^2 value of each fitting is labeled. *Right*: The best-fit total number density profiles and their comparison to the $T > 10^6$ K gas density profile in the off-filament directions in 3D (see Sect. 4.3). Different color denotes the different nearby halo masking thresholds of the stacked profiles, the same as the *left* and *middle* panels. The dashed, dash-dotted, and dotted lines denote the results of the gNFW, V06, and L23 models, respectively.

tions, reliably recover the density profiles from the cluster cores out to the circumcluster region beyond r_{200m}.

4.2. Comparison between simulations and observations

Different baryon physics models, especially the feedback models in hydrodynamic simulations, lead to large discrepancies in the gas distribution (e.g., Moser et al. 2022; Schaller et al. 2025). The profiles from the analyses of the IllustrisTNG simulation and the eRASS observations allow us to test the baryon physics models of TNG300-1 simulations. The normalization and slope of the inner profile characterize the spatial distribution of hot gas within the halo, reflecting its thermodynamic structure and underlying thermal and non-thermal effects. The outer profile reflects both the amounts of hot gas and gas-rich halos in the circumcluster or filament regions. We note that the comparison with simulations in this work is only qualitative, as the selection function of eROSITA is not applied to the simulation cluster sample.

We first compare the projected X-ray emission profile Σ_X between observations and simulations in the left panel of Fig. 7. The eRASS observed Σ_X profile (purple error bars) is the total S_X profile with the best-fit uncorrelated component (see Sect. 3) subtracted and converted using Eq. 6. It includes both the one-halo and the two-halo components. In addition to the TNG300-1 simulations analyzed here, we include a comparison with two The Three Hundred (THE300) profiles reported by Li et al. (2025), from the Gizmo-Simba and Gadget-X runs (shown as dashed and dotted green lines, respectively). The same panel also displays the TNG300-1 simulation Σ_X profile, with a nearby halo masking threshold of $10^{14} M_\odot$ in the cyan shaded region. In the inner region $r \lesssim r_{200m}$, the TNG300-1 Σ_X profile is more centrally peaked compared to the stacked observations. In the radius range of $1-4 r_{200m}$, the normalization of the TNG300-1 profile is a factor of 3 lower than the observations. This difference can be partly attributable to the limited projection depth of the TNG300-1 analysis (20 Mpc), which substantially reduces the projected two-halo signal.

Although the three simulation profiles are all calculated at $z = 0$ and with a nearby halo masking threshold of $M_{500c} = 10^{14} M_\odot$, the emissivity profiles of the two THE300 simulations have normalizations higher than those in the TNG300-1 in cluster outskirts to the circumcluster region, as shown in the left panel of Fig. 7. This could be partially attributed to the mass difference of the sample and the mass exclusion limit of the surrounding infalling halos. THE300 simulations only include massive halos with $M_{200c} > 10^{14.8} M_\odot$, whose halo bias is higher than the sample used in the TNG300-1. However, the one order of magnitude difference between the two profiles, Gizmo-Simba and Gadget-X runs, is only due to the different simulation settings. As reported by Li et al. (2025), the Gadget-X run contains a higher fraction of dense gas at large radii. The comparison of the three profiles in large radii suggests that the different adoptions of simulation codes, physical models, and model parameters could lead to a significant difference in the intensity of the circumcluster X-ray emission. The new stacked observations of the eROSITA clusters allow us to test the physical models in these unexplored regions from cluster far outskirts towards connecting filaments.

As the next step, in the right panel of Fig. 7, we compare the one-halo term density profile from the eROSITA observations with the TNG300-1 $T > 10^6$ K hot gas density profiles in the off-filament direction. As also shown in the Σ_X profile comparison, the observed gas density profile is less centrally peaked than that predicted by the TNG300-1 simulation, suggesting that feedback processes in cluster-scale halos may be stronger and more efficient than those implemented in the IllustrisTNG model, displacing part of the gas toward the cluster outskirts. Similar discrepancies have been reported at lower halo masses in the galaxy group regime. The stacked kinematic SZ (kSZ) signal of luminous red galaxies measured by ACT appears more extended than the IllustrisTNG predictions (Hadzhiyska et al. 2024). Similarly, the eROSITA-selected galaxy groups tend to exhibit higher entropy from r_{2500c} to r_{500c}, corresponding to a lower central gas density compared to the MillenniumTNG simulations (Bahar et al. 2024), whose feedback model is similar to that of the TNG300-

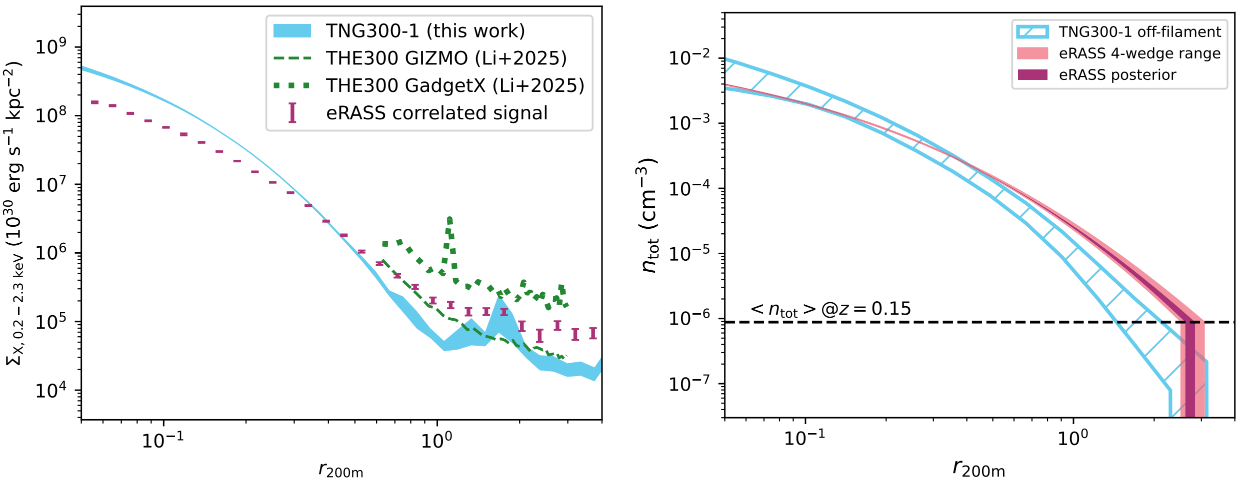

Fig. 7. *Left*: Comparison of the projected emission profiles from observations and simulations. The observed stacked eROSITA profile from this work is shown in purple error bars. The profiles extracted from the TNG300-1 simulation are shown as a cyan band. The TNG300-1 profile is more centrally peaked than the observed profile. For an additional comparison, profiles of The Three Hundred Gizmo-Simba and Gadget-X simulations from Li et al. (2025) are shown as dashed and dotted green lines, respectively. *Right*: Best-fit gNFW gas number density profile 1σ posterior range (purple) and the range of individual fittings of the four wedges (red). We overplot the scatter of the TNG300-1 gas number density profile in the off-filament directions (cyan hatched region).

1 simulations used in this work. These results are also consistent with the systematically elevated normalization of the halo $L_X - M$ relation (Pop et al. 2022) and the higher gas mass fractions within r_{500c} of the optically selected groups (Popesso et al. 2024). A detailed study of gas distribution with AGN feedback models across a large mass range of eROSITA-selected galaxy clusters and groups will be presented in our upcoming studies (Ding et al. in prep., Clerc et al. in prep.).

4.3. Thermodynamic profiles in 3D

In this section, we investigate the gas thermodynamic properties from the halo center to accretion regions in the TNG300-1 simulations. We extracted gas particles out to 5 r_{200m}, and created masks for particles belonging to nearby halos and subhalos.

The spherically averaged gas density profiles from the cluster outskirts out to several r_{200m} from hydrodynamic simulations consistently find that the profiles steepen from the cluster center to around r_{200m}, before flattening again due to the influence of cosmic filaments (O'Neil et al. 2021; Angelinelli et al. 2022; Towler et al. 2024). However, in the following, we shall argue that at the radii with the presence of cosmic filaments, the gas properties towards the into-filament and off-filament (or into-void) environments could be significantly different and cannot be reflected by the spherically averaged profiles. Therefore, we aim to explore these quantities in both the filament and off-filament directions. Following Mansfield et al. (2017) and Aung et al. (2021), we adopted an $N_{side} = 8$ HEALPix scheme to group particles into 768 directions with respect to the halo center. For each LOS direction, we binned the volume-averaged radial profiles of T, K_e, P_{gas}, and n_{tot} using 20 logarithmically spaced bins from 0.01 to 5 r_{200m}. The temperature range of $10^5 - 10^{5.5}$ K is usually the boundary between cool-to-warm and warm-hot gas (e.g. Cen & Ostriker 1999; van de Voort et al. 2011). Here we adopted a temperature threshold of 10^5 K to classify them into the in-filament and off-filament LOS directions. The into-filament/off-filament LOS profiles are those with the last radial bin temperature higher/lower than 10^5 K.

Fig. 8 shows the 68% scatter of the 768 × 159 LOS profiles of T, K_e, P_{gas}, and n_{tot} in the two different directions, where nearby $M_{500c} > 10^{13} M_\odot$ (sub)halos are excluded. For all the thermodynamic quantities of T, K_e, and P_{gas}, the into-filament and off-filament LOS profiles agree with each other within r_{200m} and show a strong discrepancy beyond that radius. The into-filament temperature profiles keep $T \sim 10^6$ K out to the maximum radius we extracted, while the off-filament-direction temperature profiles have more than two orders of magnitude drops at the radii of their accretion shocks, $\sim 2 - 3$ r_{200m}. Similarly, the discrepancy between the two directions and the feature of the accretion shock is also presented in the K_e and P_{gas} profiles. The n_{tot} profile in the two directions deviates at r_{200m}, but neither shows a jump at the shock radii. The absence of a strong jump in the total gas number density but a sharp drop in temperature is compatible with the Rankine-Hugoniot shock conditions, which impose limits of $\lim_{\mathcal{M}\to\infty} \rho_2/\rho_1 = 4$ on the density jump and $\lim_{\mathcal{M}\to\infty} T_2/T_1 = 5/16 \times \mathcal{M}^2$ on the pressure jump. For a high-$\mathcal{M}$ accretion shock, the temperature can be enhanced by more than one order of magnitude, but the density enhancement is limited to 4. This change is smaller than the scatter of LOS n_{tot} profiles among the cluster sample and could be easily smeared out due to the triaxiality of the shock surface. We additionally plot the off-filament direction gas number density profiles using gas cells with $T > 10^6$ K, which is the temperature range of X-ray-emitting gas. The gas number density profiles of the $T > 10^6$ K phase follow the total gas number density profile up to the termination at the accretion shock, which reflects that the hot gas in the off-filament direction is confined by the accretion shock. Outside the accretion shock, all gas is in temperatures lower than 10^6 K. This behavior matches the order-of-magnitude drop in the temperature profile.

5. Discussion

5.1. Characteristic radii at the halo boundary

One important question for studying halos and structure formation is where the boundary of a halo lies. The infall, orbit, and

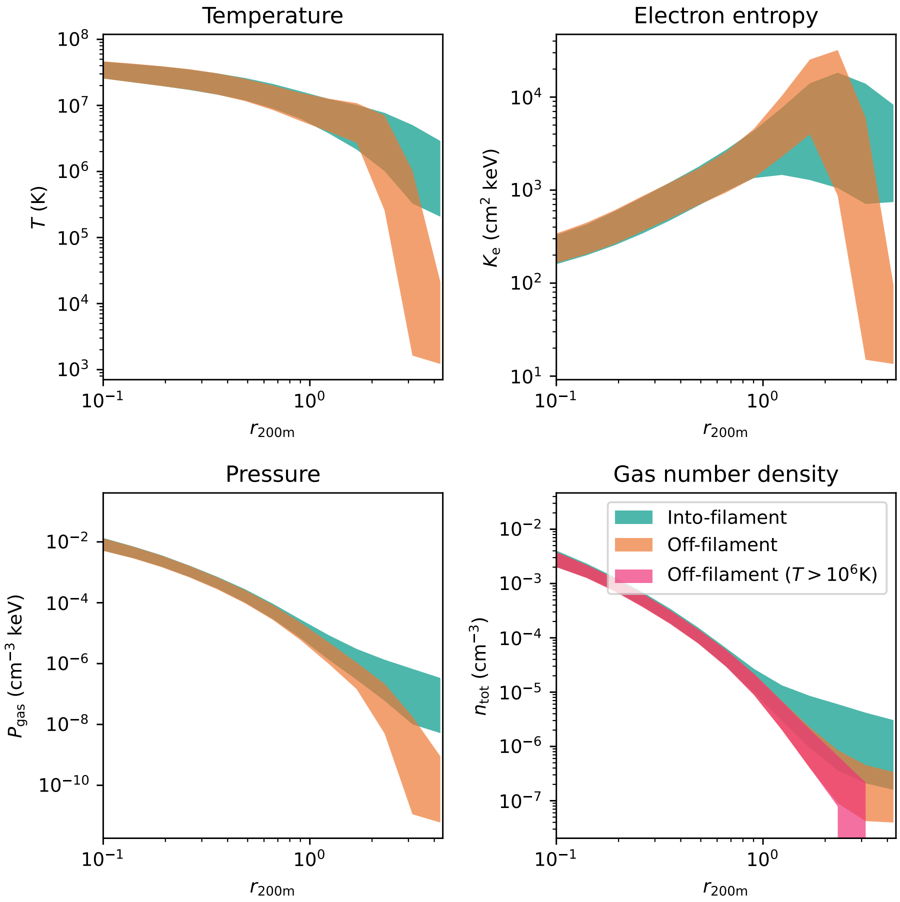

Fig. 8. One-σ scatter of the temperature (top left), electron entropy (top right), gas pressure (bottom left), and gas density (bottom right) line of sight profiles grouped into the filament (teal color) and off-filament directions (orange color) in the TNG300-1 simulations. All four types of profiles show a strong discrepancy in the two different directions. In addition, we plot the $T > 10^6$ K gas density profile in the off-filament direction in magenta in the bottom right panel. The hot gas is confined by the accretion shock within $3 \times r_{200\mathrm{m}}$.

turnaround of collisionless dark matter causes the splashback feature, which is now being widely considered as a novel definition of the halo boundary. However, the infall of collisional gas does not exhibit the splashback feature because it gets shocked before it can enter the halo. In this section, we discuss the possible characteristic radii of the gas content that can be constrained by our observations and that could be used as halo boundaries, the gas fraction enclosed in this radius, and the implications of these results.

The most prominent feature from both theoretical calculations and numerical simulations, which can be used as the halo gas boundary, is the accretion shock. In fact, the accretion shock in simulations is a gigantic structure enclosing the nodes, filaments, and sheets (e.g. Ryu et al. 2003; Schaal et al. 2016). For halos of galaxy clusters, in particular, our analysis of the LOS dependent thermodynamic profiles using TNG300-1 shows that the accretion shock is the boundary of hot gas in the off-filament direction.

In contrast to numerical simulations, it is extremely difficult to measure the distance of the accretion shock in observations from the cluster cores. For example, Anbajagane et al. (2022) presented an SZ staking study but found only a marginal feature attributed to an average accretion shock at $4.6 \times r_{200\mathrm{m}}$. The projected surface brightness profile of the stacked eROSITA observations itself (see the left panel of Fig. 7) shows no clear surface brightness features corresponding to the accretion shock beyond r_{200m}. Nevertheless, the profile fitting in this work provides an indirect clue to the accretion shock location. The TNG300-1 gas density profile in the off-filament direction (see the bottom right panel of Fig. 8) shows that the hot gas density at the accretion shock is about 2×10^{-7} cm^{-3}, slightly lower than the cosmic mean baryon density $\langle \rho_\mathrm{b} \rangle$. It proves that our assumption of gas density at the accretion shock in Eq. 3 is reasonable. From our fitting results, the gas density profile of the one-halo term reaches the $\langle \rho_\mathrm{b} \rangle$ at $\sim 3 \times r_{200\mathrm{m}}$, indicating a possible accretion shock radius based on our assumption. Moreover, the estimated shock radius is close to that from the TNG300-1 simulation (see the right panel of Fig. 7). Again, we clarify that the best-fit density profile of the one-halo term is mostly constrained by the emission at $r < r_{200\mathrm{m}}$, and the profile beyond $r_{200\mathrm{m}}$ is an extrapolation following the gNFW formalism. Nevertheless, the accretion shock remains located at $r_\mathrm{shock} \sim 3 r_{200\mathrm{m}}$, unless the density gradient undergoes a significant change in the off-filament direction beyond $r_{200\mathrm{m}}$.

Though the accretion shock is a prominent feature separating the void and the overdense cosmic web, mass accretion of galaxy clusters is mostly from the connected cosmic filaments. The high velocity infalling flows from cosmic filaments penetrate the outer atmosphere of the halo (e.g. Malavasi et al. 2023; Vurm et al. 2023; Rost et al. 2024). The model fitting of our observed profile directly reflects the radius of the halo-filament connection. In Fig. 4, the one-halo and two-halo terms intersect at $\sim 0.9 r_{200\mathrm{m}}$, shifting to $\sim 1.1 r_{200\mathrm{m}}$ if we assume that 50% of the two-halo emission originates from nearby gas-rich halos. We could therefore still conclude that $r_{200\mathrm{m}}$ approximately marks the halo–filament connection radius. Our analysis of the TNG300-1 simulation also suggests that the pressure and density LOS profiles in the filament direction deviate from those in the off-filament direction at roughly $r_{200\mathrm{m}}$. Our results of halo-filament connection radius are close to the "gas splashback radius" reported by O'Neil et al. (2021); Towler et al. (2024), who used the criteria of the steepest slope of radial gas density profile in the logarithmic space to characterize the radius. We argue that the presence of the steepest slope is necessary but not sufficient for claiming a splashback feature. The splashback is only a feature for collisionless dark matter particles; the reported steepest slope is due to the presence of nearby filaments that flatten the spherically averaged radial density profile. Meanwhile, the halo-filament connection radius at $r_{200\rm m}$ is approximately the inner shock location reported by Anbajagane et al. (2022, 2024) and the polarized stacked radio emission reported in Vernstrom et al. (2023), suggesting the discovered shock signal is due to the gas inflows from cosmic filaments.

5.2. Emission from the unvirialized gas in the two-halo term

The shock-heated gas in cosmic filaments contributed to the largest baryon budget in the late Universe (e.g. Cen & Ostriker 1999; Shull et al. 2012; Tuominen et al. 2021). However, conducting a baryon census of these gases using X-rays is challenged by the undetected nearby gas-rich halos. The density of the gas hosted in nearby halos is higher than the average value of filament gas, resulting in a significant contribution to the total filament X-ray emission. With the two-halo model formalism in this work, we investigated the fraction of the X-ray emission in the circumcluster filaments from the gas in unmasked halos.

The two-halo formalism in Eqs. 8 and 9 are theoretical calculations of the emission from nearby unmasked halos. The normalization parameter $A_{2\rm h}$ in Eq. 10 takes the additional emission from unvirialized gas in filaments into account when fitting the stacked profile. It reflects the ratio between total X-ray emission and halo X-ray emission in the two-halo term and can be converted to the fraction of halo and unvirialized gas emission components in the two-halo term.

$$f_{2\rm h}^{\rm halo} = A_{2\rm h}^{-1} \tag{15}$$

$$f_{2\rm h}^{\rm unvirialized} = 1 - A_{2\rm h}^{-1} \tag{16}$$

For our best-fit $\log A_{2\rm h} = 0.37 \pm 0.06$, the corresponding $f_{2\rm h}^{\rm unvirialized} = 0.57 \pm 0.05$.

We note that the estimation of 60% of the unvirialized gas emission fraction is based on the models of the Tinker et al. (2010) halo bias b, the Tinker et al. (2008) HMF, and the Bulbul et al. (2019) $L_{\rm X} - M$ relation. Different adoptions of the three models could result in different $f_{2\rm h}^{\rm unvirialized}$ values. We use different model combinations to recalculate the theoretical normalizations of the two-halo term and investigate the impact on the $f_{2\rm h}^{\rm unvirialized}$. We tested additional HMF models from Watson et al. (2013), and Bocquet et al. (2016), Despali et al. (2016); additional halo bias models from Bhattacharya et al. (2011), Comparat et al. (2017), Pillepich et al. (2010); additional scaling relation model from Lovisari et al. (2020) and Chiu et al. (2022). In Figure 9, we plot the calculated non-halo emission fraction with all model combinations. We found that the $f_{2\rm h}^{\rm unvirialized}$ is in a wide range from 0.18 to 0.79, and is sensitive to the adoption of the scaling relation and halo bias models. Nevertheless, the tests using those model combinations all suggest that the emission from nearby unmasked halos cannot represent the total two-halo term emission from fitting, illustrating the great potential and necessity of investigating the physical properties of the low-density unvirialized gas in these regions with the next generation X-ray missions, such as NewAthena (Cruise et al. 2025).

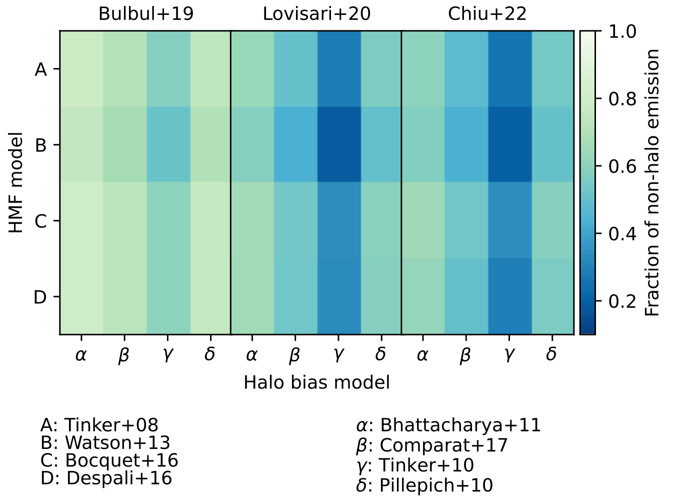

Fig. 9. Estimated emission fraction of unvirialized gas in the two-halo term using different halo mass function, halo bias, and X-ray scaling relation models. The three panels denote the three $L_{\rm X} - M$ scaling relation models; the Roman letters denote halo mass function models; and the Greek letters denote halo bias models.

5.3. Gas fraction out to $r_{200\rm m}$

The reported gas mass fraction of halos within $r_{500\rm c}$ is lower than the cosmic baryon fraction, and the depletion of the gas content is a function of halo mass (see the review of Eckert et al. 2021, and references therein). With the best-fit gas density profile in Sect. 3, we can measure the baryon density and therefore mass distribution beyond $r_{500\rm c}$ by calculating a gas mass fraction profile.

The gas fraction is defined as

$$f_{\rm gas}(r) \equiv \frac{M_{\rm gas}(r)}{M_{\rm tot}(r)}, \tag{17}$$

where $M_{\rm gas}(r)$ and $M_{\rm tot}(r)$ are the gas mass and total mass within the radius r. We estimated $M_{\rm tot}(r)$ by assuming that the total mass of the halo follows an NFW profile. Due to the self-similar properties of the NFW model, the matter density profile in units of spherical overdensity radii only depends on the concentration parameter.

Fig. 10 shows the gas fraction profile with respect to the cosmic baryon fraction with the adoption of $c_{200\rm c}$ in [3,5] in the magenta band. With the assumption of $c_{200\rm c} = 4$, the enclosed gas fraction at $r_{500\rm c}$ is $\sim$ 75% of the cosmic baryon fraction. Given the median mass $M_{500\rm c} = 2.6 \times 10^{14} M_\odot$ of our sample, the estimated $f_{\rm gas,r500c}$ value agrees with the trend from group size halos (Sun et al. 2009; Lovisari et al. 2015; Bahar et al. 2022; Bulbul et al. 2024; Siegel et al. 2025) to massive halos (Bulbul et al. 2012; Eckert et al. 2019; Bulbul et al. 2019; Liu et al. 2022; Bulbul et al. 2024). The gas fraction profile continuously increases beyond $r_{500\rm c}$, reaching a gas fraction of $\gtrsim$ 90% of the cosmic baryon fraction at $r_{200\rm m}$. Since the stellar mass fraction amounts to only a few to ten percent of the cosmic baryon fraction (e.g. Gonzalez et al. 2013), we find that the total baryon fraction within $r_{200\rm m}$, including the X-ray emitting gas and stellar fraction, is approximately equal to the cosmic value.

We compare our results with the TNG300-1 and Magneticum numerical simulations. For TNG300-1, we calculate $f_{\rm gas}$ for 159 galaxy clusters and show the 1σ scatter as the blue hatched band in Fig. 10. For Magneticum, we use the halo gas fraction profile reported by Angelinelli et al. (2022), shown as the green solid

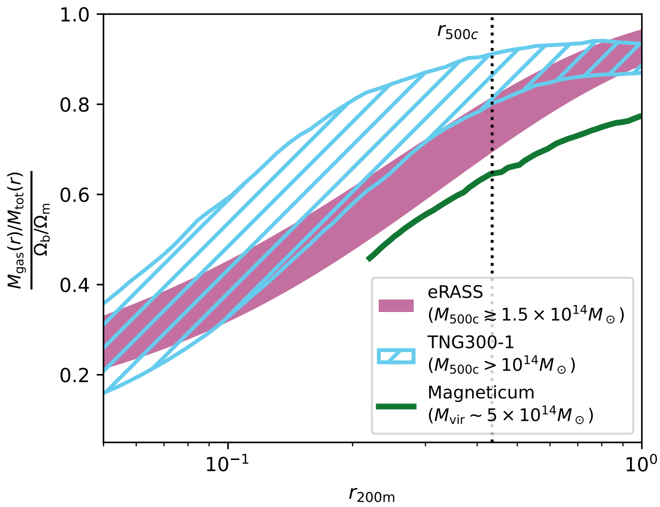

Fig. 10. Measured eROSITA gas fraction profiles with respect to the cosmic baryon fraction up to r_{200m} and the comparison with simulations. The observed profile from observation is plotted in the purple band, where the width represents the uncertainty from halo concentration c_{200c} assumptions of from 3 to 5. The 1σ scatter of gas fraction profiles of $M_{500c} > 10^{14}M_\odot$ halos in the TNG300-1 simulations is plotted in a blue hatched band. The median profile of $M_{vir} \sim 5\times10^{14}M_\odot$ mass bin in the Magneticum simulation from Angelinelli et al. (2022) is plotted as a green line.

line in Fig. 10. Specifically, we adopt the f_{gas} profile from their second most massive bin, corresponding to $M_{vir} \sim 5\times10^{14}M_\odot$. The f_{gas} profiles from the two different simulations show a distinctive difference. The TNG300-1 f_{gas} profiles reach the enclosure radius between r_{500c} and r_{200m}, while the Magneticum f_{gas} profile is much flatter than those from the TNG300-1. Although at r_{200m} the gas fraction from the TNG300-1 simulation agrees with observations within the uncertainties from assumed concentration values and cluster mass range, the slope of the TNG300-1 f_{gas} profile is different from the observation at all radii. The Magneticum simulation, on the other hand, though its gas fraction at r_{200m} is 20−30% less than the observation, its trend of the growth of the gas fraction agrees more with the observation. We note that in this work, we do not apply the correction of the clumping effects. If there is 20 − 30% clumping factor, the observed f_{gas} profile will be in line with the Magneticum simulations, whose gas fraction at r_{200m} is below 0.8 of the cosmic baryon to total matter mass ratio.

Moreover, we note an important caveat: beyond the systematic uncertainties in the total mass profile arising from the assumed concentration parameter ($c_{200c} = [3, 5]$), the gas mass profile is subject to additional systematics not included in the total error budget. In particular, in this work, the conversion from gas density to X-ray emissivity relies on the assumption of a constant cooling function. If, however, the true gas metallicity in the outskirts is lower than the assumed value, which is supported by numerical simulations, this would lead to an underestimation of both the gas mass profile and the gas fraction.

6. Conclusions

This study investigates the distribution of shock-heated gas from the outskirts of galaxy clusters into the large-scale accretion regions. We performed a stacking analysis of the two-year eROSITA All-Sky survey observations of 680 galaxy clusters selected in X-rays from the eRASS1 survey, spanning a mass range of $M_{500c} \gtrsim 10^{14}M_\odot$ and a redshift interval of $0.03 < z < 0.2$ (Bulbul et al. 2024). At the $1-2\times r_{200m}$ ($\sim 2.3-4.5$ Mpc) radii, we detect a statistically significant 12σ excess X-ray signal above the background. This represents the first detection of X-ray emission associated with galaxy clusters into the accretion region at large radii.

We model the stacked surface brightness profile as a superposition of one-halo, two-halo, and constant components, corresponding respectively to X-ray emission from the primary cluster halo, correlated structures such as infalling halos and filamentary gas, and the uncorrelated foreground/background. The best-fit results show that at r_{200m}, the gas density is $\sim 2.5\times10^{-5}$ cm^{-3}, corresponding to a baryon density constrast of $\sim$ 30. Comparing the deprojected gas density profile derived from the one-halo term of the virialized gas to previous results in the literature, in the inner regions $r < 0.1\times r_{200m}$, the profile shows slightly lower gas densities than those reported by Ghirardini et al. (2019) and L23, likely due to differences in the sample selection. In the intermediate radii, between $0.4\times r_{200m}$ and $0.6\times r_{200m}$ (approximately r_{500c} to r_{200c}), our results are consistent with those reported in the literature. The transition between the one-halo and two-halo regimes occurs around $\sim r_{200m}$, suggesting that beyond this radius, the observed signal primarily is from unvirialized gas in connected filaments and nearby halos, under the detection limit of eROSITA.

We analyzed the TNG300-1 simulation to investigate the anisotropic distribution of the intracluster and circumcluster gas and to compare it with the observations. The thermodynamic profiles of the shock heated gas exhibit clear directional dependence relative to the cosmic filaments. Along off-filament directions, the high-entropy, hot gas is sharply truncated and confined by the accretion shock at $r > r_{200m}$. In contrast, profiles along filament directions remain elevated out to the maximum extraction radius, consistent with continuous gas inflow from the cosmic filament. Furthermore, we employ the TNG300-1 data to validate our modeling framework of the stacked eROSITA observations. Incorporating a two-halo term that accounts for shock-heated gas and X-ray halos in filaments results in a best-fit one-halo profile that accurately recovers the gas density profile in off-filament directions.

The observed gas density profile is more extended, while the predicted by the TNG300-1 numerical simulations show concentrated profiles. This trend is also reflected in the gas fraction profile of the stacked cluster of galaxies. The observed gas fraction profile reaches approximately 90% of the cosmic baryon fraction at r_{200m}, indicating the baryon enclosure at such radius. The gas fraction profile of the TNG300-1 cluster sample exhibits a steep rise beyond $> 0.1r_{200}$ compared to the observations and reaches 90% cosmic baryon fraction between r_{500c} and r_{200m}. The differences in observed density and gas fraction profiles suggest that the feedback processes in $M_{500c} > 10^{14}M_\odot$ halos may be stronger than modeled in IllustrisTNG if the selection effects are ignored. This behavior is consistent with the recently observed trends at lower mass halos in galaxy group regimes in ACT kSZ measurements (Hadzhiyska et al. 2024; Siegel et al. 2025) and the stacked eROSITA observation of X-ray and optically selected galaxy groups (Bahar et al. 2024; Popesso et al. 2024).

We also explore the fractions of the two-halo emission that originates from infalling nearby halos and the low-density unvirialized filament gas in the circumcluster medium. By comparing the best-fit two-halo normalization with the predicted value using models of halo bias, halo mass function, and halo mass to luminosity scaling relations, we find that $\sim 40\%$ of the two-halo emission could be from nearby halos. However, with further exploration of the parameter space of the model choice, the fraction varies from 20% to 80%.

Comparing observations with simulations, we identify two characteristic radii in the cluster outskirts in the accretion region that signify transitions in the thermodynamic state of the intracluster and intergalactic gas, potentially defining physical halo boundaries in this region. The first is the halo–filament intersection radius, located at approximately $r_{200\mathrm{m}}$, where the two-halo term for the unvirialized gas and infalling halos in the filaments begins to dominate the stacked X-ray surface brightness profile over the one-halo term of the virialized intracluster gas, corresponding to the scale at which the gas density and pressure profiles along cosmic filament directions exceed those in the off-filament directions in the TNG300-1 simulations. The second is the accretion shock radius, estimated to lie at $\sim 3\times r_{200\mathrm{m}}$, inferred by extrapolating the one-halo gas density to the cosmic mean baryon density, consistent with the simulation predictions from the IllustrisTNG. However, the current depth of the eROSITA All-Sky Survey and the background levels limit our study to exploring the regions beyond $r_{200\mathrm{m}}$ and directly detecting the features of the accretion shock.

This work presents the eRASS stacking analysis of the shock-heated gas in cluster far outskirts and surrounding circumcluster accretion regions. The results represent the average properties of the sample studied here. Detailed studies on individual systems require high sensitivity, low instrumental background, an understanding of the foreground/background large-scale structure, and deep exposure. The upcoming NewAthena mission (Nandra et al. 2013; Cruise et al. 2025) in the late 2030s will be particularly well-suited for such targeted studies of individual galaxy clusters, providing new insights into the cluster–filament connection, the anisotropic distribution of gas at cluster boundaries, and the emission contribution from unvirialized gas within filaments.

Acknowledgements. The authors acknowledge Lars Hernquist and Volker Springel for helpful discussions. This work is based on data from eROSITA, the soft X-ray instrument aboard SRG, a joint Russian-German science mission supported by the Russian Space Agency (Roskosmos), in the interests of the Russian Academy of Sciences represented by its Space Research Institute (IKI), and the Deutsches Zentrum für Luft- und Raumfahrt (DLR). The SRG spacecraft was built by Lavochkin Association (NPOL) and its subcontractors, and is operated by NPOL with support from the Max Planck Institute for Extraterrestrial Physics (MPE). The development and construction of the eROSITA X-ray instrument was led by MPE, with contributions from the Dr. Karl Remeis Observatory Bamberg & ECAP (FAU Erlangen-Nuernberg), the University of Hamburg Observatory, the Leibniz Institute for Astrophysics Potsdam (AIP), and the Institute for Astronomy and Astrophysics of the University of Tübingen, with the support of DLR and the Max Planck Society. The Argelander Institute for Astronomy of the University of Bonn and the Ludwig Maximilians Universität Munich also participated in the science preparation for eROSITA. The eROSITA data shown here were processed using the eSASS/NRTA software system developed by the German eROSITA consortium. X. Zhang, E. Bulbul, E. Artis, and S. Zelmer acknowledge financial support from the European Research Council (ERC) Consolidator Grant under the European Union's Horizon 2020 research and innovation program (grant agreement CoG DarkQuest No 101002585). A.L. acknowledges the support from the National Natural Science Foundation of China (Grant No. 12588202). A.L. is supported by the China Manned Space Program with grant no. CMS-CSST-2025-A04.

References

Adhikari, S., Dalal, N., & Chamberlain, R. T. 2014, J. Cosmology Astropart. Phys., 2014, 019
Anbajagane, D., Chang, C., Baxter, E. J., et al. 2024, MNRAS, 527, 9378
Anbajagane, D., Chang, C., Jain, B., et al. 2022, MNRAS, 514, 1645
Angelinelli, M., Ettori, S., Dolag, K., Vazza, F., & Ragagnin, A. 2022, A&A, 663, L6
Angelinelli, M., Ettori, S., Vazza, F., & Jones, T. W. 2021, A&A, 653, A171
Arnaud, M., Pratt, G. W., Piffaretti, R., et al. 2010, A&A, 517, A92
Aung, H., Nagai, D., & Lau, E. T. 2021, MNRAS, 508, 2071
Bahar, Y. E., Bulbul, E., Clerc, N., et al. 2022, A&A, 661, A7
Bahar, Y. E., Bulbul, E., Ghirardini, V., et al. 2024, A&A, 691, A188
Baxter, E. J., Adhikari, S., Vega-Ferrero, J., et al. 2021, MNRAS, 508, 1777
Bertschinger, E. 1985, ApJS, 58, 39
Bhattacharya, S., Heitmann, K., White, M., et al. 2011, ApJ, 732, 122
Bocquet, S., Saro, A., Dolag, K., & Mohr, J. J. 2016, MNRAS, 456, 2361
Brunner, H., Liu, T., Lamer, G., et al. 2022, A&A, 661, A1
Bulbul, E., Chiu, I. N., Mohr, J. J., et al. 2019, ApJ, 871, 50
Bulbul, E., Liu, A., Kluge, M., et al. 2024, A&A, 685, A106
Bulbul, E., Randall, S. W., Bayliss, M., et al. 2016, ApJ, 818, 131
Bulbul, G. E., Hasler, N., Bonamente, M., & Joy, M. 2010, ApJ, 720, 1038
Bulbul, G. E., Smith, R. K., Foster, A., et al. 2012, ApJ, 747, 32
Cen, R. & Ostriker, J. P. 1999, ApJ, 514, 1
Chang, C., Baxter, E., Jain, B., et al. 2018, ApJ, 864, 83
CHEX-MATE Collaboration, Arnaud, M., Ettori, S., et al. 2021, A&A, 650, A104
Child, H. L., Habib, S., Heitmann, K., et al. 2018, ApJ, 859, 55
Chiu, I. N., Ghirardini, V., Liu, A., et al. 2022, A&A, 661, A11
Churazov, E., Khabibullin, I., Bykov, A. M., Lyskova, N., & Sunyaev, R. 2023, A&A, 670, A156
Clerc, N., Comparat, J., Seppi, R., et al. 2024, A&A, 687, A238
Comparat, J., Merloni, A., Ponti, G., et al. 2025, A&A, 697, A173
Comparat, J., Prada, F., Yepes, G., & Klypin, A. 2017, MNRAS, 469, 4157
Cooray, A. & Sheth, R. 2002, Phys. Rep., 372, 1
Cruise, M., Guainazzi, M., Aird, J., et al. 2025, Nature Astronomy, 9, 36
Dembinski, H., Ongmongkolkul, P., & et al. 2020
Despali, G., Giocoli, C., Angulo, R. E., et al. 2016, MNRAS, 456, 2486
Dey, A., Schlegel, D. J., Lang, D., et al. 2019, AJ, 157, 168
Diemand, J. & Kuhlen, M. 2008, ApJ, 680, L25
Diemer, B. 2018, ApJS, 239, 35
Diemer, B. 2022, MNRAS, 513, 573
Diemer, B. & Joyce, M. 2019, ApJ, 871, 168
Diemer, B. & Kravtsov, A. V. 2014, ApJ, 789, 1
Diemer, B., Mansfield, P., Kravtsov, A. V., & More, S. 2017a, ApJ, 843, 140
Diemer, B., Sparre, M., Abramson, L. E., & Torrey, P. 2017b, ApJ, 839, 26
Diemer, B., Stevens, A. R. H., Forbes, J. C., et al. 2018, The Astrophysical Journal Supplement Series, 238, 33
Eckert, D., Ettori, S., Pointecouteau, E., et al. 2017, Astronomische Nachrichten, 338, 293
Eckert, D., Gaspari, M., Gastaldello, F., Le Brun, A. M. C., & O'Sullivan, E. 2021, Universe, 7, 142
Eckert, D., Ghirardini, V., Ettori, S., et al. 2019, A&A, 621, A40
Eckert, D., Molendi, S., Vazza, F., Ettori, S., & Paltani, S. 2013, A&A, 551, A22
Eckert, D., Roncarelli, M., Ettori, S., et al. 2015, MNRAS, 447, 2198
Fillmore, J. A. & Goldreich, P. 1984, ApJ, 281, 1
Foster, A. R. & Heuer, K. 2020, Atoms, 8, 49
García, R., Salazar, E., Rozo, E., et al. 2023, MNRAS, 521, 2464
Ghirardini, V., Bulbul, E., Artis, E., et al. 2024, A&A, 689, A298
Ghirardini, V., Eckert, D., Ettori, S., et al. 2019, A&A, 621, A41
Gonzalez, A. H., Sivanandam, S., Zabludoff, A. I., & Zaritsky, D. 2013, ApJ, 778, 14
Gouin, C., Gallo, S., & Aghanim, N. 2022, A&A, 664, A198
Grandis, S., Ghirardini, V., Bocquet, S., et al. 2024, A&A, 687, A178
Hadzhiyska, B., Ferraro, S., Ried Guachalla, B., et al. 2024, arXiv e-prints, arXiv:2407.07152
Ishiyama, T., Prada, F., Klypin, A. A., et al. 2021, MNRAS, 506, 4210
Jeffreys, H. 1961, Theory of Probability, International series of monographs on physics (Clarendon Press)
Karamanis, M., Beutler, F., Peacock, J. A., Nabergoj, D., & Seljak, U. 2022a, MNRAS, 516, 1644
Karamanis, M., Nabergoj, D., Beutler, F., Peacock, J., & Seljak, U. 2022b, The Journal of Open Source Software, 7, 4634
Kass, R. E. & Raftery, A. E. 1995, Journal of the american statistical association, 90, 773
Kleinebreil, F., Grandis, S., Schrabback, T., et al. 2025, A&A, 695, A216
Kluge, M., Comparat, J., Liu, A., et al. 2024, arXiv e-prints, arXiv:2402.08453
Lau, E. T., Nagai, D., Avestruz, C., Nelson, K., & Vikhlinin, A. 2015, ApJ, 806, 68
Li, R., Cui, W., Liu, A., et al. 2025, arXiv e-prints, arXiv:2503.05011
Liu, A., Bulbul, E., Ghirardini, V., et al. 2022, A&A, 661, A2
Lodders, K., Palme, H., & Gail, H. P. 2009, Landolt Börnstein, 4B, 712
Lovisari, L., Reiprich, T. H., & Schellenberger, G. 2015, A&A, 573, A118
Lovisari, L., Schellenberger, G., Sereno, M., et al. 2020, ApJ, 892, 102
Lyskova, N., Churazov, E., Khabibullin, I. I., et al. 2023, MNRAS, 525, 898

Malavasi, N., Aghanim, N., Tanimura, H., Bonjean, V., & Douspis, M. 2020, A&A, 634, A30
Malavasi, N., Sorce, J. G., Dolag, K., & Aghanim, N. 2023, A&A, 675, A76
Mansfield, P., Kravtsov, A. V., & Diemer, B. 2017, ApJ, 841, 34
Marinacci, F., Vogelsberger, M., Pakmor, R., et al. 2018, MNRAS, 480, 5113
McCall, H., Reiprich, T. H., Veronica, A., et al. 2024, A&A, 689, A113
Merloni, A., Lamer, G., Liu, T., et al. 2024, A&A, 682, A34
Mirakhor, M. S. & Walker, S. A. 2020, MNRAS, 497, 3204
Moser, E., Battaglia, N., Nagai, D., et al. 2022, ApJ, 933, 133
Nagai, D., Kravtsov, A. V., & Vikhlinin, A. 2007, ApJ, 668, 1
Nagai, D. & Lau, E. T. 2011, ApJ, 731, L10
Naiman, J. P., Pillepich, A., Springel, V., et al. 2018, MNRAS, 477, 1206
Nandra, K., Barret, D., Barcons, X., et al. 2013, arXiv e-prints, arXiv:1306.2307
Nelson, D., Pillepich, A., Springel, V., et al. 2018, MNRAS, 475, 624
Okabe, N., Reiprich, T., Grandis, S., et al. 2025, arXiv e-prints, arXiv:2503.09952
O'Neil, S., Barnes, D. J., Vogelsberger, M., & Diemer, B. 2021, MNRAS, 504, 4649
Ostriker, J. P. & McKee, C. F. 1988, Reviews of Modern Physics, 60, 1
Pillepich, A., Nelson, D., Hernquist, L., et al. 2018, MNRAS, 475, 648
Pillepich, A., Porciani, C., & Hahn, O. 2010, MNRAS, 402, 191
Planck Collaboration, Ade, P. A. R., Aghanim, N., et al. 2013, A&A, 550, A131
Planck Collaboration, Ade, P. A. R., Aghanim, N., et al. 2016a, A&A, 594, A27
Planck Collaboration, Ade, P. A. R., Aghanim, N., et al. 2016b, A&A, 594, A13
Planck Collaboration, Aghanim, N., Akrami, Y., et al. 2020, A&A, 641, A6
Pop, A.-R., Hernquist, L., Nagai, D., et al. 2022, arXiv e-prints, arXiv:2205.11528
Popesso, P., Biviano, A., Marini, I., et al. 2024, arXiv e-prints, arXiv:2411.16555
Predehl, P., Andritschke, R., Arefiev, V., et al. 2021, A&A, 647, A1
Reiprich, T. H., Basu, K., Ettori, S., et al. 2013, Space Sci. Rev., 177, 195
Rost, A., Kuchner, U., Welker, C., et al. 2021, MNRAS, 502, 714
Rost, A. M., Nuza, S. E., Stasyszyn, F., et al. 2024, MNRAS, 527, 1301
Rykoff, E. S., Rozo, E., Busha, M. T., et al. 2014, ApJ, 785, 104
Ryu, D., Kang, H., Hallman, E., & Jones, T. W. 2003, ApJ, 593, 599
Schaal, K., Springel, V., Pakmor, R., et al. 2016, MNRAS, 461, 4441
Schaller, M., Schaye, J., Kugel, R., Broxterman, J. C., & van Daalen, M. P. 2025, MNRAS, 539, 1337
Shi, X. 2016, MNRAS, 461, 1804
Shull, J. M., Smith, B. D., & Danforth, C. W. 2012, ApJ, 759, 23
Siegel, J., Amon, A., McCarthy, I. G., et al. 2025, arXiv e-prints, arXiv:2509.10455
Simionescu, A., Allen, S. W., Mantz, A., et al. 2011, Science, 331, 1576
Smith, R. K., Brickhouse, N. S., Liedahl, D. A., & Raymond, J. C. 2001, ApJ, 556, L91
Springel, V., Pakmor, R., Pillepich, A., et al. 2018, MNRAS, 475, 676
Springel, V., White, S. D. M., Tormen, G., & Kauffmann, G. 2001, MNRAS, 328, 726
Sun, M., Voit, G. M., Donahue, M., et al. 2009, ApJ, 693, 1142
Tacchella, S., Diemer, B., Hernquist, L., et al. 2019, MNRAS, 487, 5416
Tinker, J., Kravtsov, A. V., Klypin, A., et al. 2008, ApJ, 688, 709
Tinker, J. L., Robertson, B. E., Kravtsov, A. V., et al. 2010, ApJ, 724, 878
Towler, I., Kay, S. T., Schaye, J., et al. 2024, MNRAS, 529, 2017
Tuominen, T., Nevalainen, J., Tempel, E., et al. 2021, A&A, 646, A156
van de Voort, F., Schaye, J., Booth, C. M., Haas, M. R., & Dalla Vecchia, C. 2011, MNRAS, 414, 2458
Vernstrom, T., West, J., Vazza, F., et al. 2023, Science Advances, 9, eade7233
Vikhlinin, A., Kravtsov, A., Forman, W., et al. 2006, ApJ, 640, 691
Vurm, I., Nevalainen, J., Hong, S. E., et al. 2023, A&A, 673, A62
Walker, S., Simionescu, A., Nagai, D., et al. 2019, Space Sci. Rev., 215, 7
Walker, S. A., Fabian, A. C., Sanders, J. S., Simionescu, A., & Tawara, Y. 2013, MNRAS, 432, 554
Watson, W. A., Iliev, I. T., D'Aloisio, A., et al. 2013, MNRAS, 433, 1230
Zhang, X., Bulbul, E., Malavasi, N., et al. 2024, A&A, 691, A234
Zheng, X., Ponti, G., Freyberg, M., et al. 2024, A&A, 681, A77
Zhu, Z., Kovács, O. E., Simionescu, A., & Werner, N. 2023, A&A, 678, A122
Zhuravleva, I., Churazov, E., Kravtsov, A., et al. 2013, MNRAS, 428, 3274

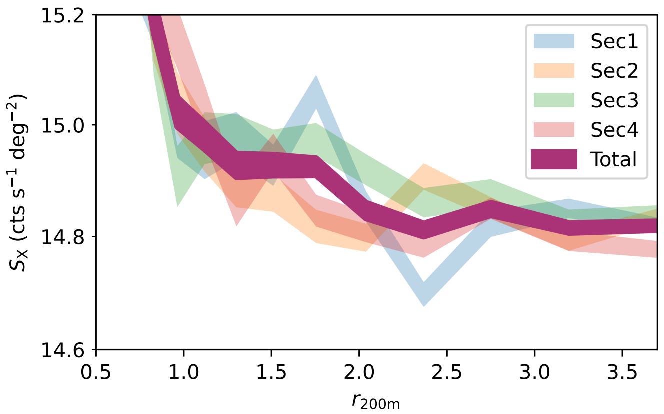

Fig. A.1. Comparison between the full stacked profile and those in four independent sectors.

Appendix A: Profiles in four individual sectors

In the inset of Fig. 3, there is a plausible surface brightness jump at $\sim 2r_{200m}$. In this section, we explore the origin of this feature.

Following L23, we divided each cluster into four 90° sectors and stacked profiles of each. The comparison between the four sector profiles and the full profile is shown in Fig. A.1. The profile in sector 1 is the most scattered profile among the four. It shows features of a spike in the bin between 1.6 and 1.9 r_{200m} and a dip in the bin between 2.2 and 2.6 r_{200m}. The two features result in a plausible jump in the full profile. Because the jump is not a universal feature in all four sectors, we do not further over-interpret it.

Appendix B: Noise level from the uncorrelated components

The stacking of randomly distributed objects in the sky is supposed to filter out the signal from uncorrelated components such as the instrumental background, sky fluctuation due to Galactic halo emission, and foreground absorption. To validate it and quantify the contribution of the uncorrelated components in the error budget, we performed stacking analysis on a source-removed sky map.

We first created an eRASS:4 HEALPix map in the 0.2-2.3 keV band with all sources removed (see Sect. 2.2.1 for the source catalogs). The example of the source masked sky rate map is shown in the left panel of Fig. B.1. Then, we randomly distributed the positions of the 680 galaxy clusters on the half-sky map. With the randomized cluster positions, we obtained a stacked surface brightness profile with the weight in Eq. 1. We repeated the randomization process 500 times to obtain a set of control sample profiles. We aim to study the relative fluctuation of each radial bin with respect to the profile average value. Therefore, for each profile, we divided it by the profile mean value to get a relative surface brightness profile. On the right panel of Fig. B.1, we show the analysis results. On the top-right panel, we plot the relative profiles of the 500 control samples, where the 68% scatter is shown as the shaded region. On the bottom-right panel, we plot the relative scatter as a function of the radius. It shows that the 680 objects and the depth of the eRASS:4 sky allow us to obtain a precision level of $< 0.3\%$ for the uncorrelated components.

Appendix C: Fitting without two-halo term

Fig. C.1 shows the best-fit components and residuals without the two-halo term. There are significant residuals at $r > r_{200m}$ in both the inset and the residual plot.

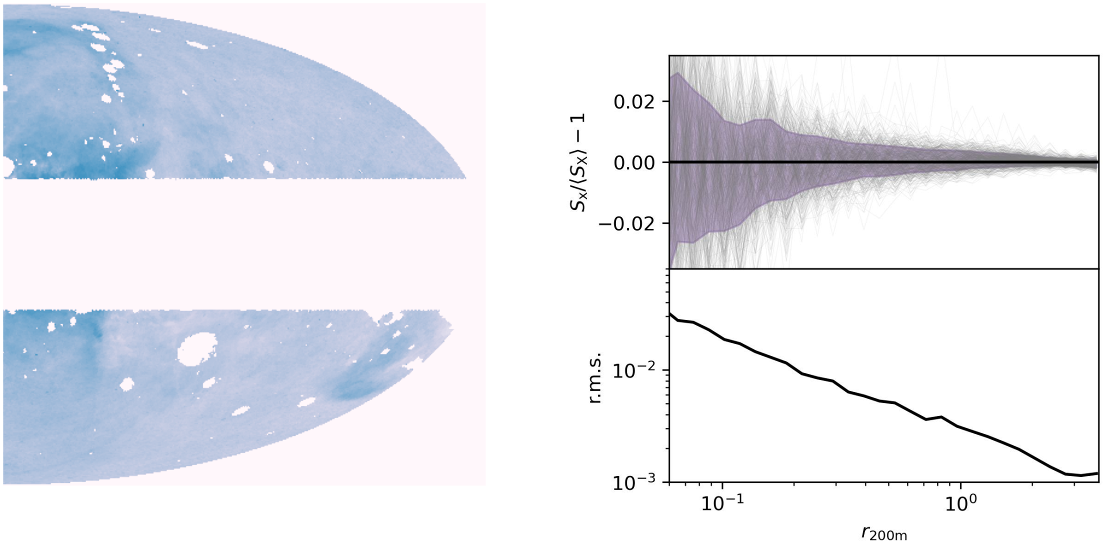

Fig. B.1. *Left*: Source removed eRASS:4 sky map for studying the uncorrelated background noise. *Top right*: Five-hundred control sample relative surface brightness profiles stacked with cluster positions randomly distributed on the sky. The shade region denotes the scatter of the 500 control sample profiles. *Bottom right*: The scatter of the 500 control sample profile as a function of the radius. As the radius increases, the scatter decreases. Beyond r_{200m}, the scatter is smaller than 0.3%

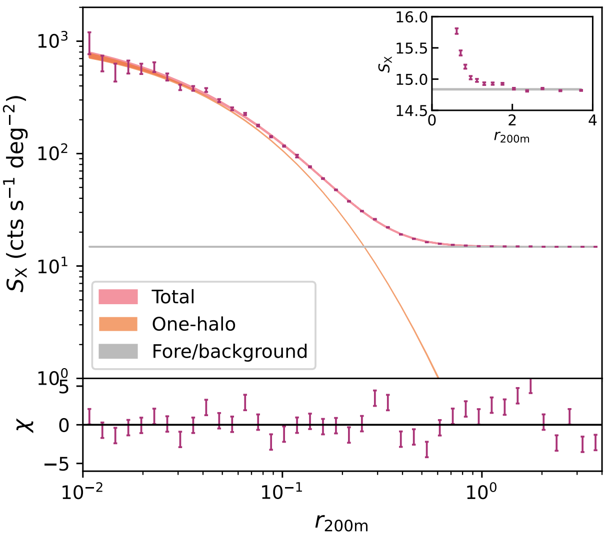

Fig. C.1. Same as Fig. 4 but without the two-halo term. Significant residuals at $r > r_{200m}$ exist.